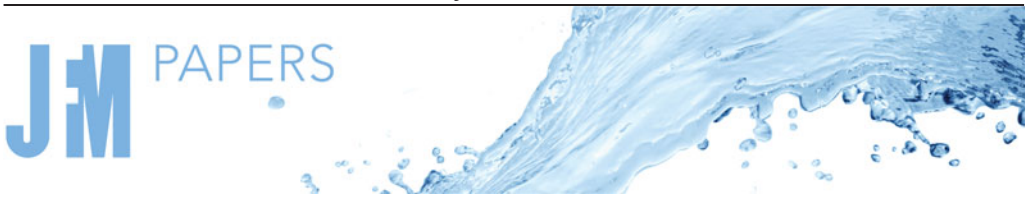
CrossMark

J. Fluid Mech. (2021), *vol*. 916, A44, doi:10.1017/jfm.2021.172



Observation-infused simulations of high-speed boundary-layer transition

David A. Buchta[1] **and Tamer A. Zaki**[1],†

[1]Department of Mechanical Engineering, Johns Hopkins University, Baltimore, MD 21218, USA

(Received 24 July 2020; revised 12 January 2021; accepted 21 February 2021)

High-speed boundary-layer transition is extremely sensitive to the free-stream disturbances which are often uncertain. This uncertainty compromises predictions of models and simulations. To enhance the fidelity of simulations, we directly infuse them with available observations. Our methodology is general and can be adopted with any simulation tool, and is herein demonstrated using direct numerical simulations. An ensemble variational (EnVar) optimization is performed, whereby we determine the upstream flow that optimally reproduces the observations. The cost functional accounts for our relative confidence in the model and the observations, and judicious choice of the ensemble members improves convergence and reduces the prediction uncertainty. We demonstrate our observation-infused predictions for boundary-layer transition at Mach 4.5. Without prior knowledge of the free-stream condition, and using only observations of wall pressure at isolated locations from an independent computation (true flow), all of the relevant inflow disturbances are identified. We then evaluate the entire flow field, beyond the original limited wall observations, and interpret simulations consistently with data and vice versa. Our predicted flow compares favourably to the true 'unknown' state, and discrepancies are analysed in detail. We also examine the impact of weighting of observations. Improved convergence of the inverse problem and accuracy of the inflow amplitudes and phases are demonstrated, and are explained by aid of a simple example from two-dimensional unstable, chaotic convection.

Key words: transition to turbulence, compressible boundary layers

1. Introduction

Accurate interpretation of wall measurements in high-speed transitional boundary layers is challenging due to sensor limitations, scarcity of data and the amplification of uncertainties – the last two factors being the focus of the present work. The acquired finite-amplitude wall signal is much smaller in dimension than the flow state; and it is the

† Email address for correspondence: t.zaki@jhu.edu

© The Author(s), 2021. Published by Cambridge University Press

https://doi.org/10.1017/jfm.2021.172 Published online by Cambridge University Press

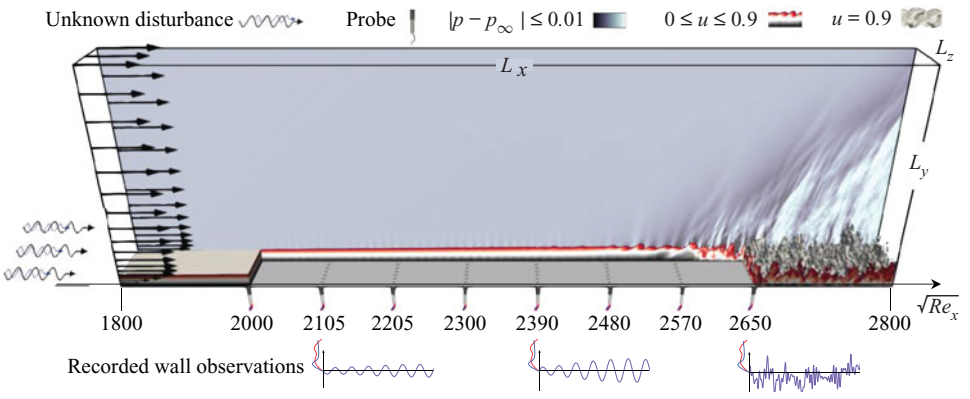


Figure 1. Flow configuration for a transitional high-speed boundary layer on a flat plate. Cutout shows the locations of discrete wall-pressure probes.

outcome of antecedent events that are governed by the Navier–Stokes equations which are chaotic and, hence, very sensitive to uncertainties. In order to optimize the interpretation of transition data, we develop an ensemble variational (EnVar) technique that infuses direct numerical simulations (DNS) with available observations, here wall-pressure data at discrete sensor locations. The data is obtained from an independent computation of $M = 4.5$ transitioning flat-plate boundary layer (see figure 1). Using our EnVar approach, we (i) identify the amplitudes and phases of unknown inflow instabilities that (ii) reproduce observations, (iii) reconstruct the full flow field beyond the spatio-temporal limits of the wall data, and (iv) decode the transition mechanism. Since the location of the wall-pressure probes encode varying levels of flow information and sensitivity, sensor weightings are considered to enhance interpretation. We provide a clear mathematical interpretation of which sensors should be discounted in order to improve accuracy.

Advances in DNS have enabled precise descriptions of hypersonic boundary-layer transition in progressively more complex regimes. For example, transition was examined on sharp (Sivasubramanian & Fasel 2015), flared (Hader & Fasel 2019) and blunted (Balakumar & Chou 2018) cones, as well as the flow over more complex geometries such as the BOLT design (Knutson, Thome & Candler 2021) including the effects of μm-sized wall roughness elements (Thome *et al.* 2018). Simulation data provide the complete space–time solution of the Navier–Stokes equations; transition mechanisms can then be directly probed and clarified. Recently, for Mach 4.5 flow, Jahanbakhshi & Zaki (2019) computed the energy transfer among wavenumber triads, as done in Cheung & Zaki (2010), to detail the mode interactions that lead to the earliest possible transition on an adiabatic flat plate. Tightly controlled DNS also provides a framework for identifying plausible hypersonic transition mechanisms (Franko & Lele 2013, 2014; Hader & Fasel 2019) and discerning valid regimes of parallel linear stability theory, linear parabolized stability equations (LPSE) and their nonlinear extension (Chang *et al.* 1993; Zhao *et al.* 2016).

Common among all simulations are assumed initial-boundary conditions, which exposes the uncertainty of how ‘real’ environmental conditions may alter transition. Often, mean inflows are based on similarity profiles of the Blasius form; yet, upstream shocks can distort the base flow and couple to boundary-layer disturbances influencing transition (Chang, Malik & Hussaini 1990; Pinna & Rambaud 2013). To consider the shock and leading edge effects, precursor simulations over the entire test article, often of lower

https://doi.org/10.1017/jfm.2021.172 Published online by Cambridge University Press

fidelity, provide the post-shock inflow state to truncated DNS domains (Li, Fu & Ma 2010; Laible & Fasel 2011; Sivasubramanian & Fasel 2015). Atop the base flow, near or at the inflow plane, space–time dependent disturbances are then introduced to seed transition. Excitation is usually a superposition of waves in one or more flow quantities: free-stream pressure (Balakumar & Chou 2018; Hader & Fasel 2018), wall-normal velocity perturbations (Li *et al.* 2010; Laible & Fasel 2011; Franko & Lele 2014; Sivasubramanian & Fasel 2015; Hader & Fasel 2019) or momentum sources (Knutson *et al.* 2021). Furthermore, the superposition is often limited to a handful of wavenumbers and frequencies. Broadband effects have also been introduced, implicitly, by pseudo random fluctuations (Li *et al.* 2010; Hader & Fasel 2018; Knutson *et al.* 2021). Similarly, transition can be triggered directly by imposing unstable mode shapes comprised of vortical, acoustic and thermal modes (Pruett & Chang 1998). While these studies expose numerous routes to turbulence, none has been directly constrained to match independent observations.

When theory or simulation conditions are incongruous with experiments, deviations are inevitable. Discrepancy often leads to speculation and errors being ascribed to uncertainty in environmental or surface conditions. Lysenko & Maslov (1984) explained the deviations in measured and theoretical instability growth rates in cooled flows, in part, in terms of the angle of waves infiltrating the boundary layer. Park & Zaki (2019) performed adjoint sensitivity analyses that detail how uncertainty in mean-velocity and temperature profiles affect growth rates; they showed that the measured growth rates by Lysenko & Maslov (1984) can result from 1 to 2 % uncertainty in wall temperature.

In another example relevant to uncertainty of inflow, DNS of $M = 6$ flow over a flared cone considered randomized inflow pressure fluctuations, in place of the free-stream disturbance environment of the tunnel (Hader & Fasel 2018). Simulations revealed agreement with the number of azimuthal high-temperature streaks to experiments as well as similar streamwise temperature variation. Together with other tightly controlled 'breakdown' simulations (Hader & Fasel 2019), the DNS provided a clear interpretation of the streak mechanism. However, the wall-pressure fluctuations for controlled breakdown DNS were over-predicted, up to 15× (Chynoweth *et al.* 2019). The forcing amplitude was selected to ensure that the nonlinear breakdown would occur in the computational domain (Hader & Fasel 2018) rather than reproducing the experimental environment. While the basic transition mechanism appears to be explained by fundamental breakdown, i.e. interacting two- and three-dimensional waves at identical second-mode frequencies, the simulations do not recover the precise experimental trajectories. Reproducing experimental measurements from all available sensor modalities would cement trust in the interpretation of data and in the computational model.

In addition to advancing direct simulations, experiments are gaining unprecedented access to hypersonic boundary-layer flow, as well as control of the flow environment and test article design (e.g. leading edge bluntness and surface roughness). Although flight tests are the ultimate target for achieving realism, flow parameters in flight (e.g. Mach and Reynolds numbers) are changing simultaneously, together with an uncertain environment, which confound predictions and interpretation of data (Thiele, Gülhan & Olivier 2018). Ground-based tests, however, offer precise control of the nominal Mach and Reynolds numbers, thereby isolating the effects of uncertain free-stream disturbances impinging on the boundary layers, as this remains a leading uncertainty in decoding transition mechanisms (Reshotko 1976; Bushnell 1990; Saric, Reed & Kerschen 2002; Schneider 2015), in part, because they are difficult to fully characterize.

Despite a looming presence of an uncertain disturbance environment, state-of-the art boundary-layer measurements illuminate hypersonic transition mechanisms. Piezoelectric pressure sensors (e.g. PCB-132) provide time resolution to detect high-frequency

https://doi.org/10.1017/jfm.2021.172 Published online by Cambridge University Press

instabilities, their harmonics and subsequent spectral broadening during transition. Marineau *et al.* (2019) provide a compilation of surface pressure measurements taken in 11 wind tunnels for $5 \leq M \leq 14$ and unit Reynolds number $1.5 \leq Re/m \leq 16$ million. In addition to PCB wall pressure identifying mode amplification rates, spatially resolved temperature measurements, using temperature sensitive paint (TSP), reveal striking, closely packed, streamwise streaks which intensify, cool and then reheat downstream on straight and flared cones in Mach 6 flow (Chynoweth 2018; Chynoweth *et al.* 2019). Additionally, time-resolved schlieren measurements (Laurence *et al.* 2012; Laurence, Wagner & Hannemann 2016; Kennedy *et al.* 2018) have quantified the structure, spectral properties and advection speed of the rope-like second-mode instabilities and their breakdown to turbulence (Casper *et al.* 2016). On more complex geometries such as BOLT, infrared cameras, PCB sensors and TSP probe the transition location and the structure of hot and cold temperature streaks in the presence of surface roughness (Berridge *et al.* 2019) and variations of free-stream disturbances found in different wind tunnels (Kostak *et al.* 2019).

Still, similar to simulations, the free-stream disturbances in experiments are a key source of uncertainty (Schneider 2001). And, when pointwise free-stream measurements are taken, for example by flow intrusive PCB enabled Pitot tubes (Bounitch, Lewis & Lafferty 2011; Masutti *et al.* 2012), complex flow interactions by preceding bow shock and a concomitant stagnation region confound interpretation of the signal, which has further spurred detailed modelling efforts using simulation (Chaudhry & Candler 2017; Duan *et al.* 2019). Recently, Parziale, Shepherd & Hornung (2014) have quantified free-stream density fluctuations using a focused laser differential interferometer (FLDI), which increases temporal and spatial resolution relative to pressure probes. Paramount, FLDI is a non-intrusive optical technique making interpretation of data straightforward relative to intrusive counterparts, and they, like schlieren, have also been successful in characterizing wave packets associated with second-mode boundary-layer instability (Parziale, Shepherd & Hornung 2015).

The hypersonics community has recognized the potential of interfacing experimental data with computations (Schneider 2015; Chynoweth *et al.* 2019; Duan *et al.* 2019). For example, comparisons with parabolized stability equations (PSE) show success for predicting instability amplification and flow structure for certain regions of measurement before transition to turbulence (Parziale *et al.* 2015; Kennedy *et al.* 2018; Marineau *et al.* 2019). Also, Duan *et al.* (2019) considered tunnel-scale simulations of the Mach 6 hypersonic Ludwieg tube, Braunschweig, which capture free-stream disturbances originating from turbulent boundary layers entering the test section. Simulations were used in tandem with free-stream pointwise measurements to characterize the spectrum, direction of incident waves and transfer function between physical waves and acquired signals. However, embedding this realism into transition models is still an active area of research. In addition, extension to hypersonic flight may be intractable, as of now, because it requires accurate precursor simulations of the flight environment in the troposphere and stratosphere. Recognizing the difficulty to fully characterize the free stream, Schneider (2015) reflects that direct simulations will need calibrated models of incoming disturbance fields from a combination of simulations and free-stream measurements.

Absent a complete characterization of the free-stream condition, the present work attempts to solve the inverse problem. Starting with available downstream observations, here wall-pressure data, we reconstruct the unknown inflow disturbance for simulations of flat-plate boundary-layer transition. The approach exploits the fact that observation data are encoded with antecedent events in the flow, which when decoded can be traced back to

https://doi.org/10.1017/jfm.2021.172 Published online by Cambridge University Press

the inflow disturbance. Once the unknown inflow is discovered, the full flow field is also available, far surpassing the domain extents and resolution of the original observations. Therefore, the approach is attractive for interpretation of flight data, e.g. reconstructing the flight environment from on-board measurements.

Section 2 introduces the ensemble variational (EnVar) framework for observation-infused simulations. The first EnVar step approximates the inflow using a linear PSE model. In this limit, the framework simplifies to a direct inversion to acquire the unknown inflow modes. The initial interpretation is further improved using EnVar iterations with DNS to extend its predictive capacity into the nonlinear regime. The results are given in § 4, and § 4.2 analyses the mechanisms for deviation between the truth and the optimally interpreted inflow. Section 5 analyses the effect of observation weighting since (i) not all sensors may yield useful inflow information, and (ii) EnVar optimization may be peculiarly sensitive to sensors recording chaotic fluctuations such as those in turbulence. Finally, discussion and conclusions are provided in § 6. Analysis of EnVar performance are provided in Appendices A and C for boundary-layer transition and unstable thermal convection, respectively.

2. Formulation of EnVar observation-infused simulations

In order to demonstrate the framework for observation-infused simulation, we adopt a canonical flat-plate boundary layer as a test bed (see figure 1). This choice enables us to relate the formulation to a physical example. However, the formulation is general, applicable to any flow configuration, available observations and numerical simulation method. Where there are elements specific to the flat-plate configuration, they are indicated as such.

We assume access to limited measurements $\boldsymbol{m}$, or observations, which will be taken to be a finite number of wall-pressure traces. We attempt to predict unknown parameters of the simulations $\boldsymbol{c}$, which will be related to the inflow disturbances. With an estimate of $\boldsymbol{c}$, we can simulate the flow using the three-dimensional Navier–Stokes equations for a calorically perfect gas, formulated in Cartesian coordinates,

$$\frac{\partial \rho}{\partial t} + \frac{\partial (\rho u_i)}{\partial x_i} = 0, \tag{2.1}$$

$$\frac{\partial (\rho u_i)}{\partial t} + \frac{\partial}{\partial x_j}(\rho u_i u_j) = -\frac{\partial p}{\partial x_i} + \frac{\partial \tau_{ij}}{\partial x_j}, \tag{2.2}$$

$$\frac{\partial E}{\partial t} + \frac{\partial}{\partial x_i}[u_i(E+p)] = \frac{\partial}{\partial x_i}(\tau_{ij} u_j) + \frac{\partial}{\partial x_i}\left(\kappa \frac{\partial T}{\partial x_i}\right), \tag{2.3}$$

where ρ is the density, u_i is the velocity in the i-th coordinate direction, p is the pressure, $E = p/(\gamma - 1) + 0.5\rho u_i u_i$ is the total energy, κ is the thermal conductivity and $T = p/(\rho R)$ is the temperature with gas constant R and ratio of specific heats γ. The components of the viscous stress tensor, assuming a Newtonian fluid, is

$$\tau_{ij} = \mu\left(\frac{\partial u_i}{\partial x_j} + \frac{\partial u_j}{\partial x_i}\right) + \left(\mu_b - \frac{2}{3}\mu\right)\delta_{ij}\frac{\partial u_k}{\partial x_k}, \tag{2.4}$$

where μ and μ_b are the shear and bulk viscosity, respectively. In compact operator form, the solution state $\boldsymbol{q} = [\rho, \rho\boldsymbol{u}, E]^{\mathrm{T}}$ which solves ((2.1)–(2.3)) is denoted as $\boldsymbol{q} = \mathcal{N}(\boldsymbol{c})$. For a linear model, e.g. PSE, we will adopt the notation $\mathcal{L}(\boldsymbol{c})$. From the flow solution, we can collect model observations $\mathcal{G}(\boldsymbol{q} = \mathcal{N}(\boldsymbol{c})) = \mathcal{M}(\boldsymbol{c})$ and compare them to $\boldsymbol{m}$. The control

https://doi.org/10.1017/jfm.2021.172 Published online by Cambridge University Press

vector and computational model should be carefully selected in order to ensure that the relevant physics are adequately captured; the present demonstration of the nonlinear EnVar technique uses DNS which ensures model adequacy.

The optimal value of the unknown $\boldsymbol{c}$ can be identified by minimizing the cost function,

$$\mathcal{J} = \tfrac{1}{2}\left\|\boldsymbol{m} - \mathcal{M}\left(\boldsymbol{c}\right)\right\|^2_{\Sigma_{\boldsymbol{m}}^{-1}} + \tfrac{1}{2}\left\|\boldsymbol{c} - \boldsymbol{c}_i\right\|^2_{\Sigma_{\boldsymbol{c}}^{-1}}. \tag{2.5}$$

The first term quantifies the deviation between observations and the model output; the second term serves to regularize the behaviour of $\mathcal{J}$ limiting how far subsequent control vectors can deviate from their initial value ($\boldsymbol{c}_i$); the $\Sigma_{\boldsymbol{m}}$ and $\Sigma_{\boldsymbol{c}}$ are the covariance matrices for the observations and control vector, respectively; and the operator $\|\cdot\|^2_{\Sigma^{-1}}$ is $(\cdot)^{\mathrm{T}}\Sigma^{-1}(\cdot)$. The covariance matrices in (2.5) serve to weight the relative trust between the data (first term) and the control vector (second term). Based on Bayes' theorem, the cost represents the negative logarithm of the posterior probability of identifying $\boldsymbol{c}$ given $\boldsymbol{m}$; this function is comprised of the likelihood of matching $\boldsymbol{m}$ given $\boldsymbol{c}$ balanced by the prior trust in $\boldsymbol{c}_i$.

An efficient approach to minimize $\mathcal{J}$ is to seek a control vector, iteratively, in the negative gradient direction $\boldsymbol{c}_{i+1} = \boldsymbol{c}_i - \gamma\nabla\mathcal{J}$ by a scalar step size γ. The evaluation of the gradient $\nabla\mathcal{J}$ can be performed using various techniques, each with advantages and drawbacks. Adjoint approaches, for example, provide an accurate gradient and their computational cost is independent of the size of the control vector; however, they require an adjoint model and storage of the forward solution, and accuracy of the forward-adjoint relation is difficult to maintain for long integration times (Vishnampet, Bodony & Freund 2015; Wang, Wang & Zaki 2019*a*; Wang & Zaki 2021). An alternative, which we adopt here, is an ensemble variational (EnVar) technique, e.g. Liu, Xiao & Wang (2008) and Mons *et al.* (2016), where an accurate approximation of the local gradient at $\boldsymbol{c}_i$ is evaluated from an ensemble of control vectors.

In EnVar, updates to the control vector $\boldsymbol{c}_i$ in the gradient direction are made by a weighted ($\boldsymbol{w}$) superposition,

$$\boldsymbol{c}_{i+1} = \boldsymbol{c}_i + \boldsymbol{P}\boldsymbol{w}, \tag{2.6}$$

where $\boldsymbol{P} = [\boldsymbol{c}^{(1)} - \boldsymbol{c}_i|\boldsymbol{c}^{(2)} - \boldsymbol{c}_i| \ldots |\boldsymbol{c}^{(N)} - \boldsymbol{c}_i]$ is a matrix with each column equal to the deviation of an ensemble member $\boldsymbol{c}^{(j)}$ from the mean $\boldsymbol{c}_i$, and $\boldsymbol{c}^{(j)}$ are sampled from a Gaussian distribution around that mean and with covariance $\Sigma_{\boldsymbol{c}}$. Note that in (2.6) the control vector is now effectively $\boldsymbol{w}$, and the gradient and step size are encoded in the matrix-vector multiplication $\boldsymbol{P}\boldsymbol{w}$, which will be discussed in detail.

Assuming that the ensemble members are small perturbations to the mean control vector, a linear approximation is valid and the model observations are expanded as

$$\mathcal{M}\left(\boldsymbol{c}\right) \approx \mathcal{M}\left(\boldsymbol{c}_i\right) + \left.\frac{\partial\mathcal{M}\left(\boldsymbol{c}\right)}{\partial\boldsymbol{c}}\right|_{\boldsymbol{c}_i}\left(\boldsymbol{c} - \boldsymbol{c}_i\right) = \mathcal{M}\left(\boldsymbol{c}_i\right) + \underbrace{\left.\frac{\partial\mathcal{M}\left(\boldsymbol{c}\right)}{\partial\boldsymbol{w}}\right|_{\boldsymbol{c}_i}}_{\boldsymbol{H}}\underbrace{\left.\frac{\partial\boldsymbol{w}}{\partial\boldsymbol{c}}\right|_{\boldsymbol{c}_i}}_{\boldsymbol{P}^{-1}}\boldsymbol{P}\boldsymbol{w}, \tag{2.7}$$

where

$$\boldsymbol{H} = \left[\mathcal{M}\left(\boldsymbol{c}^{(1)}\right) - \mathcal{M}\left(\boldsymbol{c}_i\right)|\mathcal{M}\left(\boldsymbol{c}^{(2)}\right) - \mathcal{M}\left(\boldsymbol{c}_i\right)| \ldots |\mathcal{M}\left(\boldsymbol{c}^{(N)}\right) - \mathcal{M}\left(\boldsymbol{c}_i\right)\right] \tag{2.8}$$

is the observation matrix, with columns equal to the deviation of model observations from each ensemble member and from the mean. Substitution of (2.6) and (2.7) in (2.5) yields

$$\tilde{\mathcal{J}} = \tfrac{1}{2}\left\|\boldsymbol{m} - \mathcal{M}\left(\boldsymbol{c}_i\right) - \boldsymbol{H}\boldsymbol{w}\right\|^2_{\Sigma_{\boldsymbol{m}}^{-1}} + \tfrac{1}{2}\left\|\boldsymbol{P}\boldsymbol{w}\right\|^2_{\Sigma_{\boldsymbol{c}}^{-1}}, \tag{2.9}$$

https://doi.org/10.1017/jfm.2021.172 Published online by Cambridge University Press

which is straightforward to differentiate with respect to $\boldsymbol{w}$ to obtain the gradient and Hessian,

$$\frac{\partial \tilde{\mathcal{J}}}{\partial \boldsymbol{w}} = \boldsymbol{H}^{\mathrm{T}} \boldsymbol{\Sigma}_{\boldsymbol{m}}^{-1} \left\{ \mathcal{M}\left(\boldsymbol{c}_i\right) + \boldsymbol{H}\boldsymbol{w} - \boldsymbol{m} \right\} + \boldsymbol{P}^{\mathrm{T}} \boldsymbol{\Sigma}_{\boldsymbol{c}}^{-1} \boldsymbol{P}\boldsymbol{w}, \tag{2.10}$$

$$\mathcal{H} \equiv \frac{\partial^2 \tilde{\mathcal{J}}}{\partial \boldsymbol{w}^2} = \boldsymbol{H}^{\mathrm{T}} \boldsymbol{\Sigma}_{\boldsymbol{m}}^{-1} \boldsymbol{H} + \boldsymbol{P}^{\mathrm{T}} \boldsymbol{\Sigma}_{\boldsymbol{c}}^{-1} \boldsymbol{P}, \tag{2.11}$$

which can then be adopted to minimize the cost using a variety of methods, e.g. conjugate gradient (Wang, Hasegawa & Zaki 2019*b*), L-BFGS (Wang *et al.* 2019*a*), etc. In the present study we use a Newton step, where the gradient is set to zero and corresponding weights are acquired by

$$\boldsymbol{w} = -\left(\underbrace{\boldsymbol{H}^{\mathrm{T}} \boldsymbol{\Sigma}_{\boldsymbol{m}}^{-1} \boldsymbol{H} + \boldsymbol{P}^{\mathrm{T}} \boldsymbol{\Sigma}_{\boldsymbol{c}}^{-1} \boldsymbol{P}}_{\mathcal{H}} \right)^{-1} \left(\underbrace{\boldsymbol{H}^{\mathrm{T}} \boldsymbol{\Sigma}_{\boldsymbol{m}}^{-1} \left\{ \mathcal{M}\left(\boldsymbol{c}_i\right) - \boldsymbol{m} \right\}}_{\boldsymbol{g}} \right). \tag{2.12}$$

The success of reducing $\mathcal{J}$ with the Newton step (2.12) depends, in part, on obeying the tangent approximation, and Appendix A shows the effect of nonlinearity on an EnVar gradient approximation and viable step sizes in the gradient direction. The expression (2.12), compactly expressed as $\boldsymbol{w} = -\mathcal{H}^{-1}\boldsymbol{g}$, is made of two key quantities, where $\mathcal{H}$ is the Hessian matrix of $\tilde{\mathcal{J}}$ and $\boldsymbol{g} = \nabla\tilde{\mathcal{J}}(\boldsymbol{w} = 0)$ is the gradient at the current control vector. The first factor in (2.12) has significant bearing on the difficulty, accuracy and robustness of the solution to the inverse problem. Part of the second factor indicates that the update to the previous control vector in (2.6) is proportional to the deviation between the model predictions for the mean control vector and observations. The iterative formula (2.6) continues until the cost functional reduces to a prescribed percentage of its initial value or until the change in cost stagnates.

Covariance matrices in (2.9) model the relative uncertainty, or lack of trust in the observation data and in the prior control vector. The former, $\boldsymbol{\Sigma}_{\boldsymbol{m}}$, is based on the acquisition error from diagnostic equipment, for example irreducible signal noise or the systematic error in the mathematical model to convert an electrical signal to a flow quantity. The $\boldsymbol{\Sigma}_{\boldsymbol{c}}$ reflects lack of confidence in the prior mean control vector. During an iterative optimization scheme, as $\mathcal{J}$ is progressively reduced, the trust in $\boldsymbol{c}$ should increase; thus, the $\boldsymbol{\Sigma}_{\boldsymbol{c}}$ should be reduced. In practice, at the end of each iteration, the covariance of the ensemble members is updated by taking advantage of the local shape of the cost function. Specifically, ensemble member perturbations are generated taking into account the Hessian of the cost function,

$$\boldsymbol{P}_{i+1} = \sqrt{N-1}\boldsymbol{P}_i \mathcal{H}^{-1/2} \boldsymbol{U}, \tag{2.13}$$

where $\boldsymbol{U}$ is a random, mean preserving ($\boldsymbol{U}\boldsymbol{1} = \boldsymbol{1}$), unitary ($\boldsymbol{U}^{\mathrm{T}}\boldsymbol{U} = \boldsymbol{I}$) matrix. The covariance for the $\boldsymbol{\Sigma}_{\boldsymbol{c}}$ is then updated to reflect these statistics,

$$\boldsymbol{\Sigma}_{\boldsymbol{c}}^{i+1} = \frac{1}{N-1} \boldsymbol{P}_{i+1} {\boldsymbol{P}_{i+1}}^{\mathrm{T}}. \tag{2.14}$$

A derivation of ((2.13)–(2.14)) is provided in Appendix B. Here we note that the covariance $\boldsymbol{\Sigma}_{\boldsymbol{c}}$ of the ensemble members controls the degree of satisfying the tangency approximation, and its update every iteration is influenced by the Hessian, or the local curvature of $\mathcal{J}$. Large deviations of output $\boldsymbol{H}$ (high sensitivity) implies large local curvature, which will

https://doi.org/10.1017/jfm.2021.172 Published online by Cambridge University Press

subsequently shrink control-vector variances. Although this effect will improve gradient accuracy, since subsequent ensemble members are sampled closer together, covariance shrinkage can degrade convergence rates. Shrinking control parameter variances implies increased trust in them. Thus, the second term in (2.9) outweighs the first term and data is ignored. The optimizer may appear to identify a local optimum.

In order to mitigate over shrinking control-vector covariances, Anderson & Anderson (1999) recommended multiplicative inflation, which we implement by $\boldsymbol{P}_{i+1} = \sqrt{A}\boldsymbol{P}_i$ and, thus, $\Sigma_{\boldsymbol{c}}{}^{i+1} = A/(N-1)\boldsymbol{P}_i\boldsymbol{P}_i^{\mathrm{T}}$. Covariance inflation guards against prior distributions becoming so narrow that observation data are essentially ignored, halting reduction in $\mathcal{J}$. When the cost reduction is relatively weak, we can apply covariance inflation during the EnVar procedure. Appendix C analyses the effect and shows improvement when used in conjunction with optimal sensor weighting. The EnVar approach is described in algorithm 1.

Algorithm 1: Observation-infused EnVar technique

```
Iteration i = 0
Estimate the initial control vector c_0
Generate ensemble members by sampling the normal distribution N(c_0, Σ_c)
Acquire mean model observations M(c_0)
Evaluate the initial cost J_0
while Insufficient reduction in cost do
    Acquire ensemble member model observations: M(c^(j)) | j = 1...N
    Construct observation matrix H
    Compute the gradient ∇J̃ and Hessian H
    Acquire optimal weights
    Construct the next ensemble mean c_{i+1}
    Acquire mean model observations M(c_{i+1})
    Compute the cost J and check convergence criteria
    Generate ensemble members about c_{i+1} with posterior statistics
    Update the covariance matrix Σ_c
    if Condition for covariance inflation met then
        Amplify ensemble member perturbations by √A
        Update the covariance matrix Σ_c
    end
    i = i + 1
end
Result: Optimal inflow amplitudes and phases c_opt = c_i
```

3. Simulation and optimization configuration

The ultimate future objective is to apply the observation-infused framework to experimental measurements. However, in order to fully assess performance of the method, we test our framework on observations generated from a precursor simulation. In particular, this choice facilitates precise control of the observation error, access to the true inflow disturbances and assessments of prediction accuracy beyond the measurement domain. When needed, the implications of using simulation-generated observations in place of experimental measurements, e.g. perfect vs contaminated observations, will be indicated. In our presentation of the observation-infused approach, we maintain the perspective of having access to measurements only, as in an authentic prediction, and

https://doi.org/10.1017/jfm.2021.172 Published online by Cambridge University Press

Case	M	$\sqrt{Re_{x_o}}$	L_x	L_y	L_z	N_x	N_y	N_z	T_a	Δt_a	Δt
DNS	4.5	1800	2553	200	50	1703	200	36	349	0.873	0.174
LPSE	4.5	1800	2100	200	50	85	200	36	349	0.873	—

Table 1. Simulation and data acquisition parameters.

make comparisons with the 'unknown' inflow and true flow field in § 4.2 after the EnVar optimization is completed.

For all simulations, including the precursor DNS, the computational model solves the compressible flow equations in Cartesian coordinates ((2.1)–(2.3)) for the zero-pressure gradient flat-plate boundary layer, shown in figure 1. The gas is assumed ideal with ratio of specific heats $\gamma = 1.4$ and temperature-dependent viscosity following Sutherland's formula. The flow equations are solved using a standard fourth-order Runge–Kutta scheme and interior sixth-order finite differences. Near boundaries, stencils are biased and accuracy is reduced. In the presence of shocks, a fifth-order weighted essentially non-oscillatory scheme is used locally. Detailed characterizations of the flow solver are provided elsewhere (Larsson & Lele 2009). The free-stream Mach number is $M_\infty = 4.5$, and the inflow Reynolds number is $Re \equiv \rho_\infty L U_\infty/\mu_\infty = 1800$ based on the length scale $L = \sqrt{\nu_\infty x/U_\infty}$. The computational domain size and grid resolutions are provided in table 1. In viscous units, the near-wall grid spacing is $(\Delta x^+, \Delta y^+, \Delta z^+) = (4.4, 0.25, 4.2)$.

3.1. *Precursor simulation and observations*

In practice, the geometry of the test article and the spatial distribution and type of sensors (e.g. thermocouples, PCB sensors, etc.) are known. Also another sensible expectation, the nominal flow conditions are assumed to be known, including the density ρ_∞, temperature T_∞, viscosity μ_∞ and relative velocity U_∞. Depending on the wind tunnel, a statistical characterization of the free-stream disturbances may have been made beforehand. For flight tests, a sparse historical record of atmospheric disturbances is available, but the precise state depends on the time of day and year, global position and altitude. Schneider (2001) reviews some of these relevant free-stream measurements for high-speed flight and ground-based tests; however, in the present study, no prior environmental disturbance data or physical constraints are used in the observation-infused framework.

In order to generate the surrogate observations, the precursor simulation used the spectra of the nonlinearly most dangerous inflow disturbance that was reported by Jahanbakhshi & Zaki (2019) for a Mach 4.5 boundary layer, and scaled the total energy to half their value. This configuration should be contrasted to the classical scenarios where either subharmonic or fundamental oblique waves are introduced in order to initiate secondary instability of a primary two-dimensional second mode. Transition due to our choice of inflow is more challenging to predict for the following reasons. (i) The inflow disturbance is comprised of two planar second modes and an oblique first mode (details in § 4, table 2), which do not satisfy the fundamental or subharmonic resonance criteria. (ii) The energy in these modes at the inflow is sufficiently high that nonlinear interactions are relevant early upstream. (iii) A series of nonlinear energy transfers spur new instability waves, not present at the inflow, and hence predicting the inflow by decoding downstream observations is more difficult than in classical fundamental and subharmonic transition. (iv) Transition takes place swiftly relative to those classical mechanisms. The spectra of the

https://doi.org/10.1017/jfm.2021.172 Published online by Cambridge University Press

		$\mathcal{E}_{(F,k_z)}/\mathcal{E}_o$ (%)			
Case	$\mathcal{E}_o \times 10^5$	(100, 0)	(110, 0)	(40, 1)	Other modes
*E*0	2.85	2	97	—	1
*E*1	3.40	2	80	17	1
Truth	1.00	31	26	43	—

Table 2. Distribution of modal energy.

inflow condition in the precursor simulation is the 'unknown' truth that we seek to predict. It is noteworthy that, even in the context of the precursor simulation, the sensitivities of discrete wall-pressure measurements and of transition to the inflow are not known. The EnVar algorithm, by attempting to discover the inflow condition, decodes the inflow mode amplitudes and phases that are pertinent for reproducing observations.

For the surrogate measurements $\boldsymbol{m}$, time traces of surface pressure are acquired from a regular array of 64 PCB-like sensors, $N_x^s \times N_z^s = 8 \times 8$, which is a practical number used in ground-based (Marineau *et al.* 2015; Zhu *et al.* 2016) and flight tests (Thiele *et al.* 2018). The sensor spacing is uniform in the span due to homogeneity of the flow in that dimension. In the streamwise direction physical limitations often preclude placement of the sensors far upstream. In addition, upstream sensors may suffer low signal-to-noise ratio. The N-factors for the second-mode instabilities can provide some guidance, for example to cluster the sensors at the positions where the N-factors peak, although the uncertainty of transition location motivates a uniform spacing rather than clustering. Strategies for optimal sensor placement (see, e.g. Mons, Wang & Zaki 2019) in uncertain environments are the subject of ongoing research. For the present purposes, and taking into account the above considerations, we distributed the sensors uniformly between $2000 \leq \sqrt{Re_x} \leq 2650$.

Once the flow has reached a statistically stationary state, observations were acquired for a duration $T_a = 349L/U_\infty$, which was resolved using $N_t = 400$ samples. While in physical experiments the observations may span a longer duration, even when bound by the tunnel run time, the assimilation time horizon is shorter for computational efficiency since each EnVar iteration required $N + 1 = 17$ forward simulations. The horizon is however sufficiently long to capture an adequate number of waves, and in our case spans $\gtrsim 10$ periods of the second mode. In terms of sampling rate, in physical experiments it is a limitation of the sensor. This reality was emulated by sub-sampling the simulation but ensuring that we resolve potential second-mode instabilities and nonlinearly generated harmonics. Figure 2(*a*) shows traces from probes along the fourth streamwise ray of sensors $z = 20.8$, and figure 2(*b*) shows the resolution of the acquisition sampling. The time dependent wall pressure from the sixty-four discrete sensors are then concatenated to form the observation vector,

$$\boldsymbol{m} = \left[p\left(\boldsymbol{x}^s_{1,1}, t_1\right), \ldots, p\left(\boldsymbol{x}^s_{1,1}, t_{N_t}\right), \ldots, p\left(\boldsymbol{x}^s_{N_x^s,N_z^s}, t_1\right), \ldots, p\left(\boldsymbol{x}^s_{N_x^s,N_z^s}, t_{N_t}\right)\right]^{\mathrm{T}}, \quad (3.1)$$

where $\boldsymbol{x}^s_{i,j}$ is the (x, z) position of the (i, j) sensor on the wall.

In each step of the EnVar algorithm, model observations $\mathcal{M}(\boldsymbol{q})$ are collected and compared with $\boldsymbol{m}$. This step is performed similarly to the above description, where the wall pressures are recorded at the locations of the sensors and at the same sampling rate. Note that in experiments, physical sensors may introduce additional effects, for example filtering due to finite sensor size (Kennedy *et al.* 2018). For PCB probes, corrections to

https://doi.org/10.1017/jfm.2021.172 Published online by Cambridge University Press

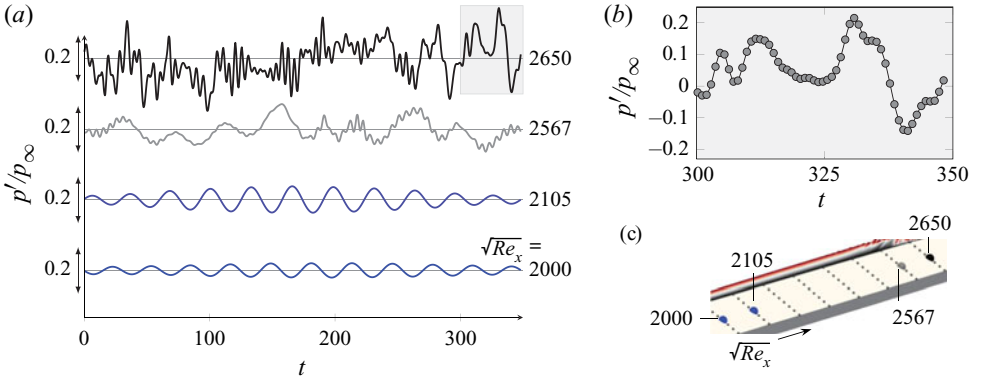


Figure 2. (*a*) Sample wall-pressure signals from the precursor DNS, extracted at $z = 20.8$ and $\sqrt{Re_x} = \{2000, 2105, 2567, 2650\}$. Horizontal lines indicate $p' = 0$. (*b*) Detail of the shaded region in (*a*); the acquisition frequency is shown by symbols. (*c*) Detail of sensor positions: large symbols correspond to traces shown in (*a*) and small symbols are remaining sensors.

the spectra have been developed (Corcos 1963; Lueptow 1995) that can be applied to $\boldsymbol{m}$ directly. Alternatively, the impact of the sensor can be incorporated in $\mathcal{M}(\boldsymbol{q})$.

3.2. *EnVar configuration*

Generally, environmental disturbances are a mixture of acoustic, vortical and entropic components (Kovasznay 1953), and in high-speed tunnels the makeup of disturbances is dominated by intense acoustic waves (e.g. Pate 1980). In the present simulation domain, we express the unknown inflow disturbance as a superposition of instability waves of the boundary layer. This choice is natural given the exhaustive literature on boundary-layer receptivity and transition mechanisms that are framed in terms of originally linear instability waves (Mack 1975; Malik 1990; Fedorov 2011). Despite our particular parameterization, the EnVar technique is amenable to other forcing schemes and can also accommodate additional uncertain parameters (e.g. surface roughness, real-gas effects, etc.).

The full inflow condition is expressed as a superposition of the mean state and instability waves,

$$\boldsymbol{q}_o = [\bar{\rho}, \bar{u}, \bar{v}, \bar{w}, \bar{T}]^{\mathrm{T}}(y) + Re\left(\sum_m \sum_f c_{f,m}[\hat{\rho}, \hat{u}, \hat{v}, \hat{w}, \hat{T}]^{\mathrm{T}}_{f,m}(y)\exp[\mathrm{i}\beta_m z - \mathrm{i}\omega_f t + \mathrm{i}\theta_{f,m}]\right). \tag{3.2}$$

In this form, the control vector is comprised of the unknown amplitudes and phases $\boldsymbol{c} = [\ldots, c_{f,m}, \theta_{f,m}, \ldots]^{\mathrm{T}}$ of the inlet instability waves. The choice of the range and the resolution of the inflow frequencies is guided by preliminary spectral analysis of the observations, which is the natural approach to adopt in practice with experimental measurements. Initially, thirty-three wavenumber-frequency pairs are considered, which encompass first- and second-mode instabilities for the range $1800 \leq \sqrt{Re_x} \leq 2650$. The non-dimensional frequencies and integer spanwise wavenumbers are

$$F = \frac{\omega_f}{\sqrt{Re_{x_o}}} \times 10^6, \quad \text{for } f \in [1, 2, \ldots, 11], \tag{3.3}$$

https://doi.org/10.1017/jfm.2021.172 Published online by Cambridge University Press

and

$$k_z = \frac{\beta_m L_z}{2\pi} = m \quad \text{for } m \in [0, 1, 2]. \tag{3.4}$$

For each (F, k_z) pair, we consider the most unstable slow modes (Fedorov 2011) at the inflow $\sqrt{Re_x} = 1800$ from the discrete Orr–Sommerfeld and Squire spectra. Note that the choice of normalizing mode shapes (e.g. $\hat{\rho}$) is not unique and can influence reproducibility. We adopt the energy normalization (Mack 1984; Hanifi, Schmid & Henningson 1996),

$$\mathcal{E}_{f,m} = \tfrac{1}{2} \int_0^{L_y} \hat{\boldsymbol{q}}^{\star} \boldsymbol{M} \hat{\boldsymbol{q}} \, \mathrm{d}y, \tag{3.5}$$

where $(^{\star})$ is the complex conjugate transpose, $\hat{\boldsymbol{q}}$ is the solution vector $[\hat{\rho}, \hat{u}, \hat{v}, \hat{w}, \hat{T}]^{\mathrm{T}}_{f,m}$, and the matrix $\boldsymbol{M}$ scales the density, momentum and internal energy by

$$\boldsymbol{M} = \mathrm{diag}\left[\frac{1}{\gamma(\gamma-1)M^2}\frac{\bar{T}}{\bar{\rho}}, \quad \bar{\rho}, \quad \bar{\rho}, \quad \bar{\rho}, \quad \frac{1}{\gamma(\gamma-1)M^2}\frac{\bar{\rho}}{\bar{T}}\right], \tag{3.6}$$

which includes the non-dimensionalization of our equations.

With all thirty-three instability waves considered, the control vector would be comprised of sixty-six unknowns. In order to reduce the dimensionality of the EnVar optimization, it is desirable to reduce the length of the control vector and to establish a good initial guess. Both objectives are achieved using a LPSE estimate of the control vector, which is discussed in § 3.3. The eight instability waves that are predicted by the LPSE estimation to have the largest inflow amplitudes will form the control vector for subsequent iterations using the nonlinear EnVar algorithm. Therefore, the number of ensemble members in the main algorithm was $N = 16$, which is the same size as the control vector. Each EnVar iteration thus involves $N + 1 = 17$ simulations, where the additional DNS corresponds to the mean of the ensemble.

The initial covariance matrices are $\boldsymbol{\Sigma_m} = \sigma_m^2 \boldsymbol{I}$, where $\sigma_m = 10^{-1.75}$ based on the intensity of the recorded pressure fluctuations ($p'_{rms} \approx 0.017$ at the first sensor row $\sqrt{Re_x} = 2000$), and $\boldsymbol{\Sigma_c} = \sigma_c^2 \, \mathrm{diag}[\boldsymbol{c_0}]^2$, where $\sigma_c = 0.4$. A preliminary test was conducted which showed that the relatively large value of σ_c yielded variation of outcomes across all of the sensor positions which was deemed sufficient for starting the EnVar procedure. Had the ensemble members yielded indistinguishable observations, perhaps from a very tight $\boldsymbol{\Sigma_c}$, the observation matrix would be nearly singular affecting optimization. Although a relatively large σ_c may violate the tangent approximation, initially, the $\boldsymbol{\Sigma_c}$ is iteratively refined by exploiting the local shape of the cost function using ((2.13)–(2.14)).

3.3. *Initial estimate of the control vector*

The EnVar algorithm requires an initial estimate of the control vector, $\boldsymbol{c}_0$. One may assume a uniform distribution of energy among all possible inflow instability waves, or a turbulent energy spectrum, or any other condition motivated by prior knowledge of the flow environment. Since the first estimate $\boldsymbol{c}_0$ has bearing on performance of the gradient-based optimization, it warrants careful consideration. Here, we present a method reliant on the LPSE. The motivation for this choice is that it provides a viable physical explanation of the observations, within a well established set of assumptions. This interpretation is valuable in itself when computational resources are not available to solve the full nonlinear problem. In addition, when sensors are in the linear disturbance regime – an assumption that we do

https://doi.org/10.1017/jfm.2021.172 Published online by Cambridge University Press

not adopt in this work – the accuracy of this inflow estimate is fully determined by the accuracy of the PSE approximation and the measurement uncertainty.

Due to linearity of PSE, each inflow instability wave evolves independently and can be considered as an ensemble member. Instead of the Navier–Stokes model, we express the LPSE as $\boldsymbol{q} = \mathcal{L}(\boldsymbol{c})$. The cost functional is then

$$\mathcal{J} = \tfrac{1}{2} \left\| \boldsymbol{m} - \boldsymbol{L}\boldsymbol{v} \right\|^2 + \frac{\varrho}{2} \left\| \boldsymbol{v} - \boldsymbol{e} \right\|^2 . \tag{3.7}$$

The columns of the matrix $\boldsymbol{L}$ have the form

$$\boldsymbol{L} = \left[\dots \mid \dots \mid \mathrm{Re}\left(\hat{p}_{f,m}\right) \mid -\mathrm{Im}\left(\hat{p}_{f,m}\right) \mid \dots \mid \dots \right], \tag{3.8}$$

with each pair being the real and imaginary parts of the Fourier transform of the observed pressure due to mode (f, m). The new control vector is therefore $\boldsymbol{v}$ whose elements $\boldsymbol{v} = [\dots, v_{f,m}, w_{f,m}, \dots]^{\mathrm{T}}$ are the unknown modal coefficients. The second term in (3.7), weighted by a scalar ϱ, accounts for prior information $\boldsymbol{e}$ regarding the disturbance environment, for example from characterization of the free-stream conditions in a tunnel or in flight. Even absent such knowledge ($\boldsymbol{e} = 0$), the second term serves to regularize the control vector such that we identify the inflow condition $\boldsymbol{v}$ that best reproduces the observations while also having a small quadratic norm. Since (3.7) is quadratic, the minimizer of $\mathcal{J}$ is obtained by taking the gradient and assuming stationarity, which yields

$$\boldsymbol{v} = \left(\boldsymbol{L}^{\mathrm{T}}\boldsymbol{L} + \varrho \boldsymbol{I}\right)^{-1} \left(\boldsymbol{L}^{\mathrm{T}}\boldsymbol{m}^{\dagger} + \varrho \boldsymbol{e}\right). \tag{3.9}$$

The estimate of the control vector (3.9) can use a subset of sensor data ($\boldsymbol{m}^{\dagger}$) that are best suited for the linear approximation of PSE. This step benefits from examination of the spectrum of the observations (see figure 5), which show the presence of fundamental frequencies, but also the signature of higher harmonics before becoming more broadband by the fourth sensor row. For our configuration, we used observations from the first row of sensors only, $\boldsymbol{m}^{\dagger} = \boldsymbol{m} \mid \sqrt{Re_x} = 2000$, and the parameters of the PSE computations are summarized in table 1. For our sensor network, the LPSE estimation yields a good estimate of the inflow condition without regularization ($\varrho = 0$), although we caution that this is not generally the case especially for a small number of sensors. For example, given only one sensor, waves with the correct frequency but any spanwise wavenumber k_z can be phase shifted and scaled to precisely match the data, yielding an infinite number of potential solutions and (3.9) becomes ill-conditioned. In that case, including ϱ ensures that the LPSE estimation selects the mode with the lowest quadratic norm.

Once $\boldsymbol{v}$ was acquired, we identified the eight largest modal amplitudes in the ranges $40 \leq F \leq 110$ and $0 \leq k_z \leq 2$. Only the associated instability waves were retained in the subsequent EnVar optimization where the initial estimate of the control vector was

$$\boldsymbol{c}_0 = \left[\dots, \sqrt{v_{f,m}^2 + w_{f,m}^2}, \tan^{-1}(w_{f,m}/v_{f,m}), \dots \right]^{\mathrm{T}}. \tag{3.10}$$

4. Results

Before reporting the predictions by the EnVar algorithm, we examine the observations, or pressure traces, without aid of the equations and attempt to identify information that may be pertinent to the transition mechanism. In particular, figure 2(*a*) shows what appears to be a single dominant instability wave at $\sqrt{Re_x} = 2000$ and broadband p' signal at $\sqrt{Re_x} = 2650$. However, Fourier analysis uncovers a richer spectrum of waves,

https://doi.org/10.1017/jfm.2021.172 Published online by Cambridge University Press

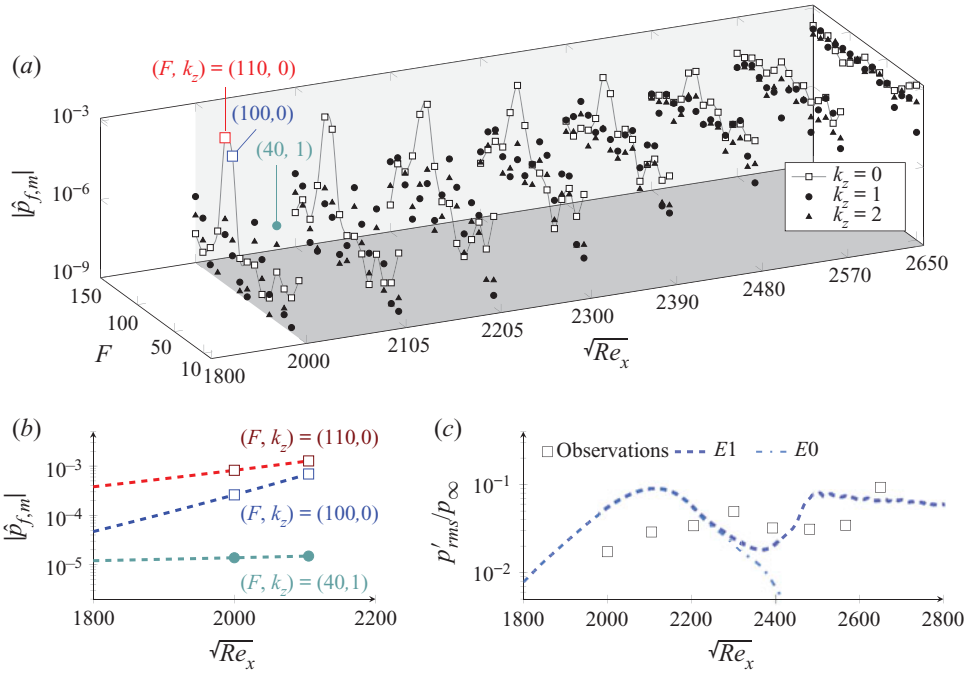


Figure 3. (*a*) Pressure spectra from the 64 sensors placed on the adiabatic wall $2000 \leq \sqrt{Re_x} \leq 2650$. Three modes with the largest amplitudes at $\sqrt{Re_x} = 2000$ are identified. (*b*) Possible inflow conditions using least-squares fit of amplitudes of those three modes at the first two sensor rows. (*c*) Wall-pressure prediction from DNS using the inflow conditions $E0$ and $E1$.

including the signature of three-dimensional ones (figure 3*a*). The peak two-dimensional instabilities, $F = 100$ and 110, amplify between $2000 \leq \sqrt{Re_x} \leq 2300$, and the signal appears to become broadband by $\sqrt{Re_x} \geq 2450$. Based on the figure and also linear PSE of the potential instability waves (performed to identify the initial guess of the EnVar algorithm), transition would be ascribed to amplifying second-mode instabilities; yet with limited information, the role that lower amplitude modes play in spurring key interactions for transition is uncertain, in fact unknown.

We will consider two estimates of the inflow condition using only the data, akin to common interpretations of experimental measurements. The purpose is to provide the backdrop for evaluating the physics-based EnVar approach. The modes that have the largest wall pressure $|\hat{p}_{f,m}|$ at $\sqrt{Re_x} = 2000$ are isolated and their streamwise development is plotted in figure 3(*b*). The first two sensor rows suggest an exponential amplification model,

$$\ln |\hat{p}_{f,m}|(x) = a_0 + a_1 x. \tag{4.1}$$

This interpretation and similar approaches in the literature are predicated on linear assumptions, namely that instability waves evolve independently and amplify exponentially. Using the above exponential model, we can infer the inlet amplitude from the sensor data. The first estimate of the inflow (case '$E0$') is comprised of the two planar waves $(F, k_z) = (100, 0)$ and $(110, 0)$, since measurements often focus on identifying planar second modes. The second estimate of the inflow (case '$E1$') also includes the oblique wave $(F, k_z) = (40, 1)$. In addition, for both $E0$ and $E1$, we assigned 1 % of

https://doi.org/10.1017/jfm.2021.172 Published online by Cambridge University Press

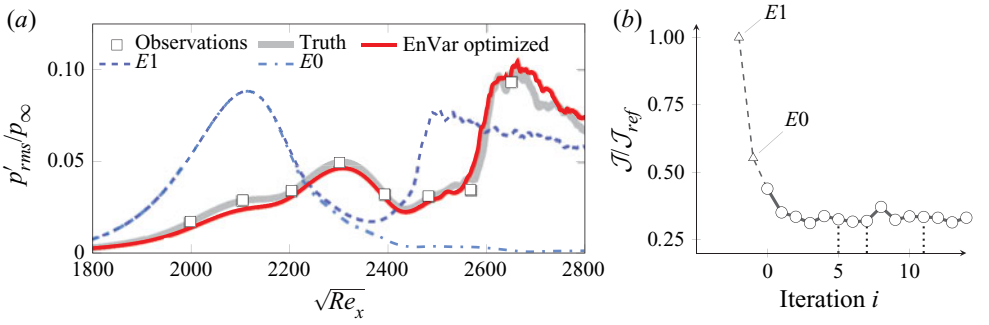


Figure 4. (*a*) Intensity of wall-pressure fluctuations. (*b*) The normalized cost function; vertical dashed lines identify iterations where Σ_c was inflated.

the total inflow disturbance energy $\mathcal{E}_o$ to all the remaining instability waves, including three-dimensional ones. Table 2 summarizes the distribution of energy for these cases.

Figure 3(*c*) shows the outcome of simulations that adopt $E0$ and $E1$ as inflow conditions. Both interpretations are incongruous with the root-mean-square (r.m.s.) of the observed wall pressure. In both cases, the r.m.s. pressure fluctuations are over-predicted by almost a factor of three, near $\sqrt{Re_x} \approx 2100$. In case $E0$ transition is entirely absent within the computational domain even though we distributed 1 % of the energy in various modes to promote secondary instability of the planar waves. When mode $(F, k_z) = (40, 1)$ is included (case $E1$), transition is premature. Worse, the cause of discrepancy is unknown and remains speculative.

Unlike the above empirical approach, we wish to minimize ambiguities of transition mechanisms and contradicting interpretations. Our approach, the observation-infused EnVar framework, seeks the unknown inflow that optimally reproduces the observations.

4.1. *Optimal interpretation from the observation-infused framework*

The optimization seeks inflow amplitudes and phases which minimize the discrepancy between the simulated and observed wall pressures, acquired from a regular array of 64 PCB-like sensors. Figure 4(*a*) contrasts the wall-pressure r.m.s. between the predictions and observations. Unlike the predictions assuming exponential amplification of modal amplitudes (cases $E0$ and $E1$), the EnVar technique identifies an inflow condition that accurately reproduces the sensor data. In fact, the observation-infused simulation tracks the pressure development even upstream, in between and downstream of the sensors and predicts transition location, far outperforming empirical interpretations.

Although, the r.m.s. is a useful statistical comparison, the optimization exploited pointwise, time-resolved observations in order to reconstruct, as close as possible, the exact state-space trajectory of the experiment. Pointwise deviations are quantified by the cost function $\mathcal{J}$ using (2.5), which is reported in figure 4(*b*) for $E0$ and $E1$, and for all iterations during the EnVar gradient-based optimization. In concurrence with figure 4(*a*), the EnVar approach improves the interpretations, although the reduction of the cost function by a factor of three appears humble relative to the improved prediction of the r.m.s. pressure fluctuations.

The small reduction of the cost functional could be a symptom of reaching a local optimum. An obvious factor is the initial estimate of the control vector, which in our case is from the PSE solution and is hence physical. Another key element is the landscape of the cost functional $\mathcal{J}$ that is being explored by the EnVar technique. The representation of the

https://doi.org/10.1017/jfm.2021.172 Published online by Cambridge University Press

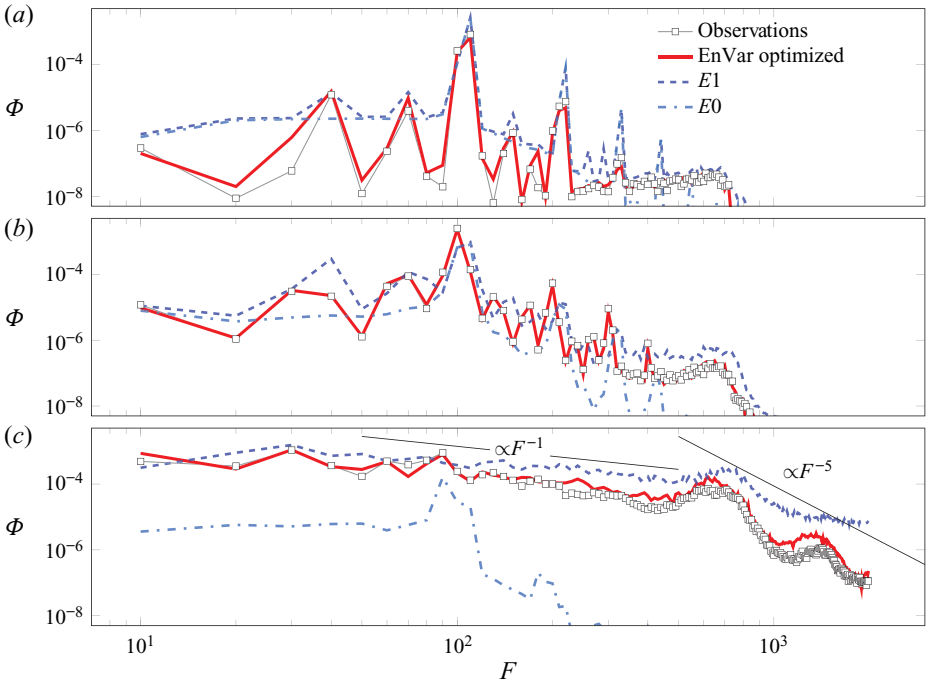


Figure 5. Wall-pressure spectra averaged in z: (*a*) first row $\sqrt{Re_x} = 2000$, (*b*) fourth row $\sqrt{Re_x} = 2300$ and (*c*) seventh row $\sqrt{Re_x} = 2570$. For reference, the F^{-1} and F^{-5} sloped lines indicate spectral roll off in equilibrium boundary-layer turbulence (Bull 1996).

landscape is partly determined by the outcomes within the observation matrix $\boldsymbol{H}$, because the variance of the ensemble members at each iteration depends on the local Hessian $\mathcal{H}$. When the surface of $\mathcal{J}$ is highly oscillatory, the variance of the ensemble reduces, the members explore a smaller region, and reduction in $\mathcal{J}$ ceases. In order to mitigate this potential issue, we have inflated the covariance of the control vector at iterations $i = 5$, $i = 7$ and $i = 11$, which were selected based on the flattening of $\mathcal{J}$. Despite the covariance inflation, the reduction rate of the cost function appears inappreciably affected. Another important factor that impacts the optimization is the shape of the cost function, which depends on the placement of sensors, their relative weighting and the relative trust in observations vs in the prior control vector. While we will not vary the placement of the sensors, we will evaluate the degree to which the present uniform sensor weighting impacts the optimization in § 5, and also using a model system in Appendix C. In particular, § 5 will introduce a weighting strategy which will achieve over two orders of magnitude cost reduction in as little as one-third of the iterations. Tests indicate that discounting the observations from sensors that contribute to the largest uncertainty in the inverse problem, through chaos, reduces the oscillations in the landscape of the cost function and improves the EnVar solution. Despite these allusions to enhancing success of EnVar, we proceed in demonstrating the best that we can achieve assuming all observations are weighted equally.

The pressure spectra provide a further refined view of the wall-pressure reconstruction, beyond the r.m.s. in figure 4. The spectra can, for example, indicate the presence of key instabilities, higher harmonics and spectral broadening possibly due to nonlinearity. Figure 5 shows the pressure frequency spectra averaged in the span across the $N_z^s = 8$

https://doi.org/10.1017/jfm.2021.172 Published online by Cambridge University Press

sensors,

$$\Phi = \frac{1}{N_z^s}\sum_{j=1}^{N_z^s}\left|\frac{1}{N_t}\sum_{n=0}^{N_t-1} p(\boldsymbol{x}_{i,j}^s, t_n)\exp\left[-\mathrm{i}\,(2\pi f/T_a)\,n\Delta t_a\right]\right|, \tag{4.2}$$

where $f = [0, 1, \ldots, N_t - 1]$ is the integer frequency. Results are reported for the first, fourth and seventh sensor rows, which respectively correspond to the early pre-transitional regime, the region near the peak r.m.s. wall pressure and the region immediately preceding transition. The EnVar optimized solution reproduces the spectral content of the observations. In figure 5(*a*) there is mild deviation for energy at frequencies $F = [20, 30, 50, 90]$, albeit relatively low amplitude, which suggests that the EnVar-estimated inflow spurs nonlinear interactions earlier than in the true flow. Yet by $\sqrt{Re_x} = 2300$, the EnVar predictions are indistinguishable from the observations. In contrast, case *E*0 that overlooks mode $(F, k_z) = (40, 1)$ does not yield amplifying instabilities $F = [30, 60, 70]$, possibly due to nonlinear interactions, and transition to turbulence is not achieved within the simulation domain. Including $(F, k_z) = (40, 1)$ in the physics-free exponential model (case *E*1) can lead to transition, but the levels in the spectra disagree with the observations (figure 5*c*), which demonstrates that the transition mechanism in such an approach is inconsistent with the true flow.

4.2. *Assessment of performance using the true state*

To this point, the accuracy of the EnVar predictions was assessed against the discrete observations, which are a subspace of the complete flow state. However, since the observations were generated from a simulation as a surrogate for experiment, we also have access to the entire true state for the purposes of benchmarking the accuracy of our predictions. In particular, transition in the true flow was caused by the nonlinear most unstable inflow comprised of modes $(F, k_z) = (40, 1)$, $(100, 0)$ and $(110, 0)$ as noted in § 3.1. We examine the details of the transition process beginning with flow-field visualizations in figure 6. The physics-free interpretations, *E*0 and *E*1, which adopt an exponential fit of the sensor data, are shown in the first two panels; they are qualitatively different from the true state (panel *d*). These results also exemplify the sensitivity of boundary-layer transition to the influence of $(F, k_z) = (40, 1)$. Lacking this particular mode (figure 6*a*) yields a persistently laminar field within the simulation domain; over-predicting the amplitude of that mode (figure 6*b*) accelerates transition significantly. Relative to the physics-free interpretations in the first two panels, the EnVar optimized simulation in panel *c* develops similarly to the truth. The formation of three-dimensional structures above the wall and transition are observed near $\sqrt{Re_x} \approx 2400$. To assess the accuracy at longer distances, the flow was simulated much farther than the domain adopted for EnVar optimization. In the turbulent regime, $3309 \leq \sqrt{Re_x} \leq 3507$, the instantaneous flow deviates from the truth due to the chaotic nature of turbulence which amplifies differences at the inflow.

An important measure of accuracy in predicting transitional flows is the ability to identify transition location. Figure 7 shows that the skin-friction coefficient, $C_f = (2/\rho_\infty U_\infty^2)\langle\tau_w\rangle_{zt}$, where $\langle\cdot\rangle_\chi$ denotes averaging in the 'χ' direction, has a similar level of agreement as the r.m.s. wall pressure in figure 4(*a*). Whether adopting wall shear-stress observations, instead of wall pressure, would yield less or more accurate predictions than in figure 7 is not a simple question for two reasons. Firstly, as a practical consideration, the errors in acquiring observations depend on the sensing modality. We are reminded, however, that this issue is mitigated here because we adopted a precursor simulation as a

https://doi.org/10.1017/jfm.2021.172 Published online by Cambridge University Press

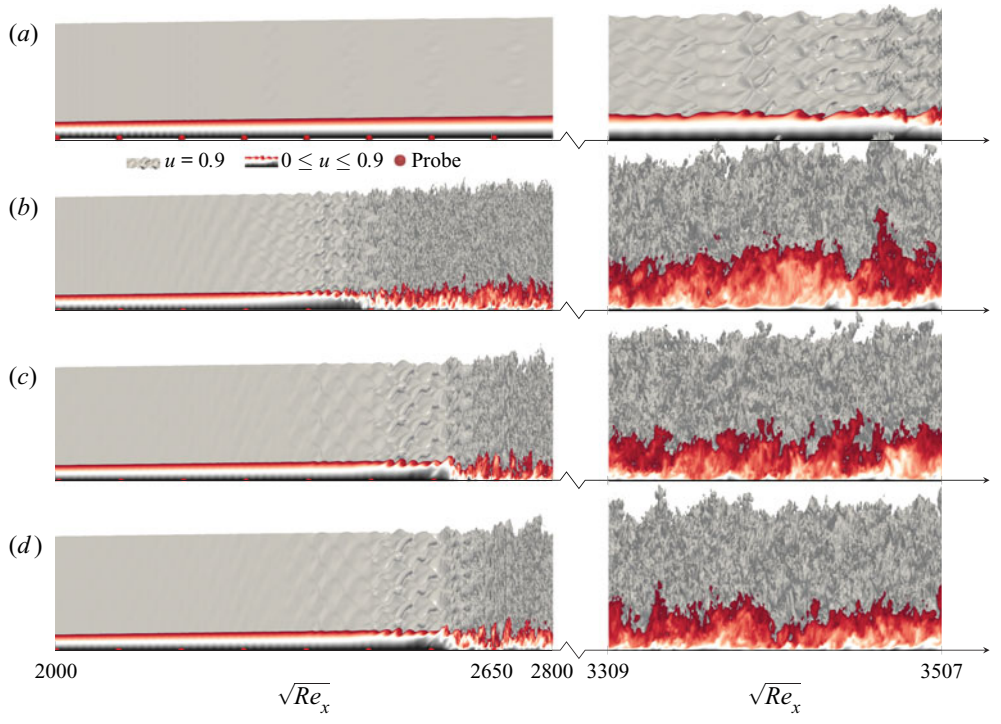


Figure 6. Visualization of streamwise velocity from DNS of (*a*) *E*0, (*b*) *E*1, (*c*) EnVar optimized inflow after 14 iterations and (*d*) true inflow condition.

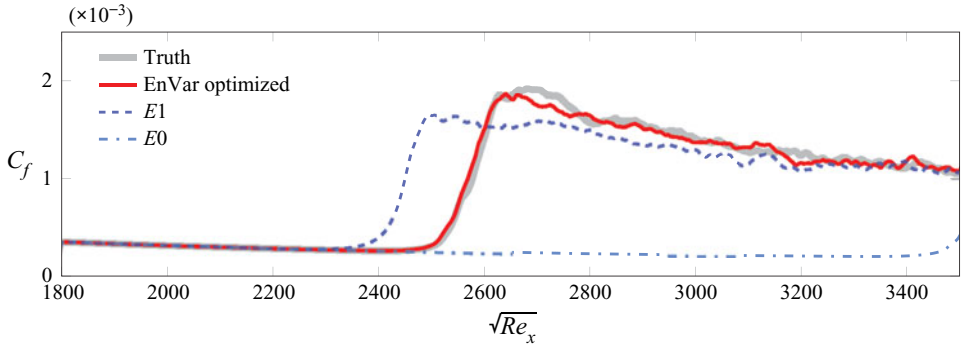


Figure 7. Downstream dependence of the mean skin-friction coefficient.

proxy for experiments, and our observations are sampled in the exact same manner as in the EnVar procedure. Secondly, and perhaps more importantly, the landscape of the cost functional changes depending on the choice of observations. The accuracy of interpreting different measurement modalities and the impact of their respective uncertainties is the subject of ongoing work.

In addition to graphs demonstrating qualitative agreement between the EnVar-estimated and true flows, we quantify the deviation between flow fields. We begin with the r.m.s. error in the wall pressure, $\epsilon_{p_w} = \sqrt{\langle (p'_w - p'^{\top}_w)^2 \rangle_{zt}}$. Figure 8 shows that inflow conditions *E*0 and *E*1 that are exponential fits from downstream sensor data lead to large errors.

https://doi.org/10.1017/jfm.2021.172 Published online by Cambridge University Press

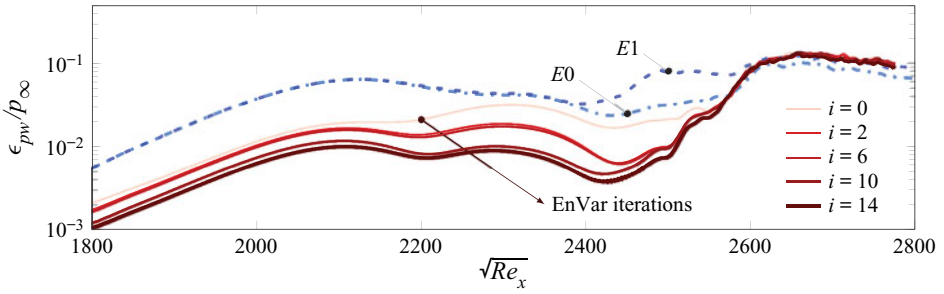


Figure 8. Wall-pressure errors for inflow conditions estimated from (solid) successive EnVar iterations $i = \{0, 2, 6, 10, 14\}$, as well as exponential modal growth models (dash–dotted) $E0$ and (dashed) $E1$.

In contrast, the EnVar technique provides the smallest wall-pressure errors, which concurs with the results in figure 4. In the region $2100 \leq Re_x \leq 2500$, nonlinear interactions lead to important energy exchanges among modes for this configuration (Jahanbakhshi & Zaki 2019). Within this region and also upstream, successive EnVar iterations progressively refine wall-pressure predictions and reduce the errors, until the point of transition to turbulence. In the turbulence ($\sqrt{Re_x} \gtrsim 2600$), the errors are commensurate with the r.m.s. pressure signal, $\epsilon_{p_w} \approx p'^{\top}_{rms}$. Although the upstream flow was captured well by the EnVar optimization, to no surprise the streamwise variation of errors increase near the turbulence since small inflow deviation (≈0.1 % wall-pressure error at $\sqrt{Re_x} = 1800$) can have a drastic impact on the instantaneous trajectory of the flow as confirmed by flow visualizations in figure 6(*c*,*d*).

The above comparison was focused on errors along the wall, the plane where the sensors were placed. Here we expand the focus to the full flow, which naturally includes regions beyond the domain of dependence of the observations. Figure 9 shows the errors in the instantaneous (*a*,*b*) pressure $\epsilon_p = \langle (p - p^{\top})^2 \rangle_z$ and (*c*,*d*) full state vector $\epsilon_q = \langle (\boldsymbol{q} - \boldsymbol{q}^{\top})^{\mathrm{T}} \boldsymbol{M} (\boldsymbol{q} - \boldsymbol{q}^{\top}) \rangle_z$, where $\boldsymbol{M}$ appropriately weights momentum, density and internal energy (see (3.6)). Near $2000 \leq \sqrt{Re_x} \leq 2400$, pressure deviations are amplifying in two regions: along the wall and then later ($\sqrt{Re_x} \gtrsim 2000$) near the boundary-layer edge $y \approx \delta_{99}$. The pressure deviation, seemingly disconnected in the two regions, appears to merge across the boundary layer to the wall by $\sqrt{Re_x} \approx 2400$ and subsequently saturates beyond $\sqrt{Re_x} \gtrsim 2600$. Instantaneous differences in the turbulence have large errors in the pressure, but this error also appears to radiate above the turbulence. The visualization is consistent with errors in the radiated Mach waves (Phillips 1960). Differences within the turbulence amount to differences in the radiated pressure as intense sound waves. When the full state vector is considered, figure 9(*c*) shows that the deviation along the boundary-layer edge is pronounced as early upstream as the inflow and more intense than at the wall $y = 0$. This pattern can arise due to a missing inflow wave that EnVar could not identify or conversely one that was predicted by EnVar but which does not exist in the true flow; the latter is indeed the case as will be clarified by the inflow spectra. The absence of a similar error pattern in the pressure suggests that the erroneous wave is vortical in nature, supported near the boundary-layer edge. These errors advect downstream, amplify and eventually spread towards the wall. The impingement onto the wall takes place near the last three wall-pressure probes $2482 \leq \sqrt{Re_x} \leq 2567$, which coincides with the intense amplification of pressure errors in figure 8(*a*). Notably, the visualization shows how inflow disturbances can elude detection from wall sensors until advection and diffusion

https://doi.org/10.1017/jfm.2021.172 Published online by Cambridge University Press

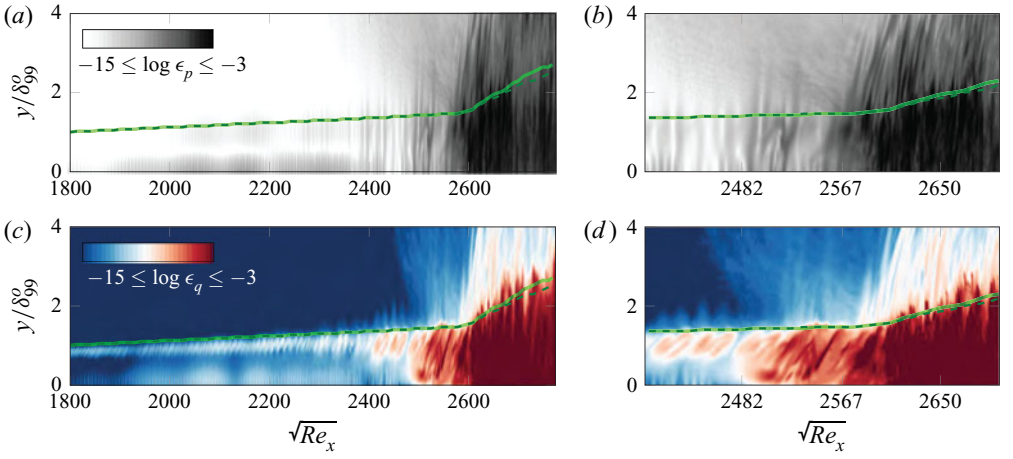


Figure 9. Instantaneous errors in EnVar-estimated flow relative to the truth. Contours show spanwise average errors in (*a*,*b*) pressure and (*c*,*d*) full state vector. Overlaid curves represent the position of $\delta_{99}(x)$ for the (solid) truth and (dashed) EnVar prediction.

spread their influence to the wall, potentially after participating in nonlinear interactions with other waves. These results motivate future work on optimal sensors placements that maximize the sensitivity of the observations to the inflow condition and also assimilation of multiple sensing modalities in $\boldsymbol{m}$, e.g. synchronous schlieren and PCB.

Since the flow is amenable to spectral analysis, we consider the two-dimensional Fourier transform in the span and in time. We begin with the development of the three true inflow modes, only, and compare against predictions in figure 10. The exponential amplification model adopted in cases $E0$ and $E1$ (panels *a*,*b*) mispredicts the inflow amplitudes of the second-mode instabilities $(F, k_z) = (100, 0)$ and $(110, 0)$. Notably, their growth rates are similar to the truth up to $\sqrt{Re_x} < 2400$. While some modes are undergoing nonlinear interactions, the second mode evolves linearly to high amplitude (not shown), which is similar to observations in previous experiment-simulation comparisons of flow over a cone (Kennedy *et al.* 2018). Without sufficient energy in $(F, k_z) = (40, 1)$ transition to turbulence is delayed beyond the simulation domain in (a), which underscores the importance of the three-dimensional waves that are often unavailable from experimental measurements and, hence, excluded from the analysis (Marineau *et al.* 2014; Kennedy *et al.* 2018; Marineau *et al.* 2019). In case $E1$ (figure 10*b*) the inflow amplitude of $(40, 1)$ was accurately predicted by the exponential amplification model and its development is indistinguishable from the truth until $\sqrt{Re_x} \approx 2100$, after which the mode amplifies intensely and transition to turbulence is accelerated. The over-prediction of $(F, k_z) = (110, 0)$, together with $(40, 1)$, spur nonlinearities earlier, specifically $(70, 1)$, $(30, 1)$, $(10, 0)$, which feed back into $(40, 1)$. Only when the amplitudes of these three main instability waves are accurately predicted, relative to the true inflow condition, do their downstream nonlinear developments agree as in figure 10(*c*).

To summarize the outcome of the EnVar estimation using equally weighted sensors, figure 11(*a*,*b*) show the amplitudes of the estimated and true inflow modes. Reported on the contours in (*a*) are percent errors in the amplitude and phase of the true inflow waves: $(\epsilon_A, \epsilon_\phi) = (19\,\%, 11\,\%)$, $(8\,\%, 6\,\%)$ and $(27\,\%, 1\,\%)$ for modes $(F, k_z) = (100, 0)$, $(110, 0)$ and $(40, 1)$, respectively. While these errors are rather large, they are important to discuss before attempting to reduce them further. Here, we only note that we will

https://doi.org/10.1017/jfm.2021.172 Published online by Cambridge University Press

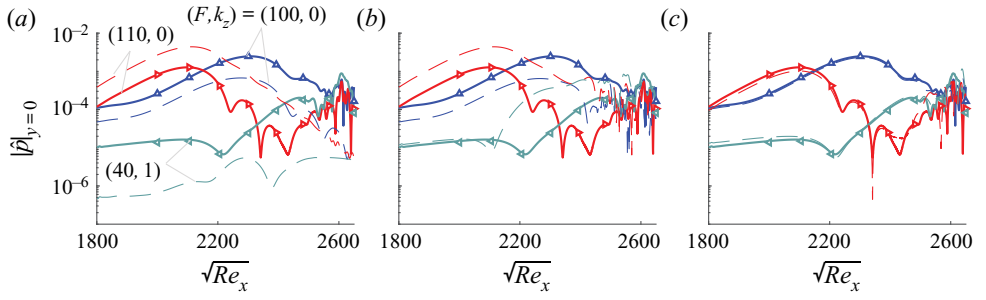


Figure 10. Streamwise development of wall-pressure spectra for (*a*) *E*0, (*b*) *E*1 and (*c*) EnVar optimized framework at iteration $i = 14$. Observations (symbols); truth (solid); model prediction (dashed).

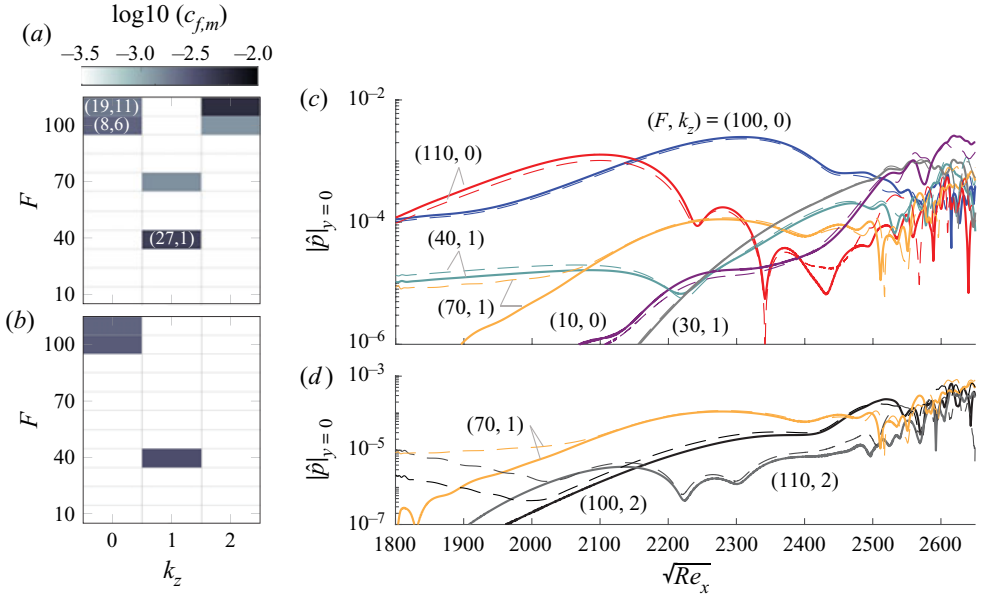


Figure 11. (*a*,*b*) Amplitudes of inflow instabilities: (*a*) EnVar, (*b*) truth. Marked values in (*a*) are the percent errors in the amplitude and phase relative to the true inflow. (*c*,*d*) Streamwise development of the wall-pressure spectra: (solid) truth; (dashed) EnVar-predicted flow after 14 iterations.

successfully mitigate these errors in the following section to much lower levels, especially for second-mode instabilities – $(\epsilon_A, \epsilon_\phi) = (1\,\%, 3\,\%)$, $(7\,\%, 3\,\%)$ and $(22\,\%, 0.9\,\%)$ – by an optimal weighting of observation stations. The large errors in the predicted inflow spectra highlight the difficulty of reconstructing the environmental disturbance from wall observations, even when the full nonlinear equations are adopted in the estimation. Even more, the results show that exceptional agreement of wall data and transition location may not translate into precise inflow interpretation. The core challenge is the nonlinear and chaotic nature of the system, for which multiple optima can confound interpretation and exacerbate the challenge of reducing inflow uncertainty. In regard to these points, we emphasize that the transition mechanism is successfully reproduced, which is shown in figure 11(*c*) for the true inflow modes $\{(100, 0), (110, 0), (40, 1)\}$. The figure also shows the evolution of three key waves $\{(70, 1), (10, 0), (30, 1)\}$ that participate in important nonlinear interactions which culminate in breakdown to turbulence (see Jahanbakhshi &

https://doi.org/10.1017/jfm.2021.172 Published online by Cambridge University Press

Zaki 2019 for detailed analysis of energy transfer among wave triads). Figure 11(*d*) focuses on the inflow modes that are not part of the truth, including $(F, k_z) = (70, 1)$ which is reproduced from panel (*c*). Notably, after a region of adjustment, all three erroneous inflow modes $\{(70, 1), (100, 2), (110, 2)\}$ latch onto the trajectories of their counterparts in the true flow. This behaviour indicates that the observations are insensitive to the inflow amplitudes of these modes, which indeed do not compromise the accuracy of reproducing the observations or the fidelity of predicting the true transition mechanism – this point will be revisited in the following section.

5. Influence of sensor weighting on optimization

In the previous section the EnVar estimation of the unknown inflow reproduced the wall-pressure observations and accurately predicted transition location and mechanism. Despite this success, the reduction in the cost function was relatively humble and the inflow spectra included appreciable errors. We contend that these symptoms are due to infusing all available observations with equal weights, some of which can negatively impact gradient-based optimization, hence confounding interpretation. Observations can provide relevant physical information to discover unknown parameters; however, their information content may be duplicate and possibly yield conflicting interpretations. Observations may also be prone to uncertainty which affect optimization techniques. These notions are all present in the mathematical formulation of the EnVar algorithm, which is influenced by the local shape of $\mathcal{J}$ and relies on its local gradient and curvature. For example, chaotic dynamics such as in boundary-layer transition and turbulence imply that small changes in the control vector can yield large deviations in the observation matrix $\boldsymbol{H}$ and, hence, appreciable reduction in the variance of subsequent ensembles; a remedy using variance inflation is thus needed.

From a geometric perspective, the chaotic dynamics also cause the surface of the cost functional to be highly oscillatory, or wrinkled. Thus, $\mathcal{J}$ will have large local curvature restricting the optimizer in a shallow local optimum. The local curvature is described by the Hessian matrix, $\mathcal{H}$, which can be decomposed as $\mathcal{H} = \boldsymbol{Q}\varLambda\boldsymbol{Q}^{-1}$, where $\varLambda = \mathrm{diag}(\lambda_1, \lambda_2, \ldots, \lambda_N)$ contains the eigenvalues and the columns of $\boldsymbol{Q}$ are the eigenvectors. We consider optimizing scalar invariants of the matrix $\varLambda$, e.g. condition number $\kappa = \lambda_{max}/\lambda_{min}$, where λ_{max} and λ_{min} are the maximum and minimum eigenvalues in $\varLambda$. To improve accuracy of inverting $\mathcal{H}$ or modify its curvature, we can manipulate the eigenspectrum (Ucinski 2004). For example, three potential strategies are to minimize κ (K-optimality) (Yan *et al.* 2018), minimize λ_{max} as will be adopted herein, maximize λ_{min} (E-optimality) (Colburn 2011; Wilson, Schultz & Murphey 2014).

To adjust the eigenvalue spectrum of $\mathcal{H}$, we consider its two terms due to the observations ($\boldsymbol{H}^{\mathrm{T}}\boldsymbol{\Sigma}_{\boldsymbol{m}}^{-1}\boldsymbol{H}$) and the prior ($\boldsymbol{P}^{\mathrm{T}}\boldsymbol{\Sigma}_{\boldsymbol{c}}^{-1}\boldsymbol{P}$). In general, we have flexibility to adjust each term. For example, the measurement covariance $\boldsymbol{\Sigma}_{\boldsymbol{m}}$ can be made so large that all of the data are ignored and only the ensemble member control vectors affect the $\mathcal{H}$. In practice however, the measurement error $\boldsymbol{\Sigma}_{\boldsymbol{m}}$ is an outcome of irreducible signal noise and errors in the model that transforms the sensor signal into the observed flow quantity. Therefore, increasing observation covariance is unjustified. Here we consider applying weights selectively to the observations, in both $\boldsymbol{m}$ and $\boldsymbol{H}$. With the applied weights, $\mathcal{H}$ can be reconstructed and its eigenvalue spectrum analysed. The weights are then adjusted until the eigenvalue spectrum has a desired property, e.g. minimizing the maximum eigenvalue of $\mathcal{H}$ thereby reducing extreme curvature. We emphasize that this scheme does not target flattening the cost functional in all control-vector directions; such a strategy would lead to significant uncertainty in the solution of the optimization problem.

https://doi.org/10.1017/jfm.2021.172 Published online by Cambridge University Press

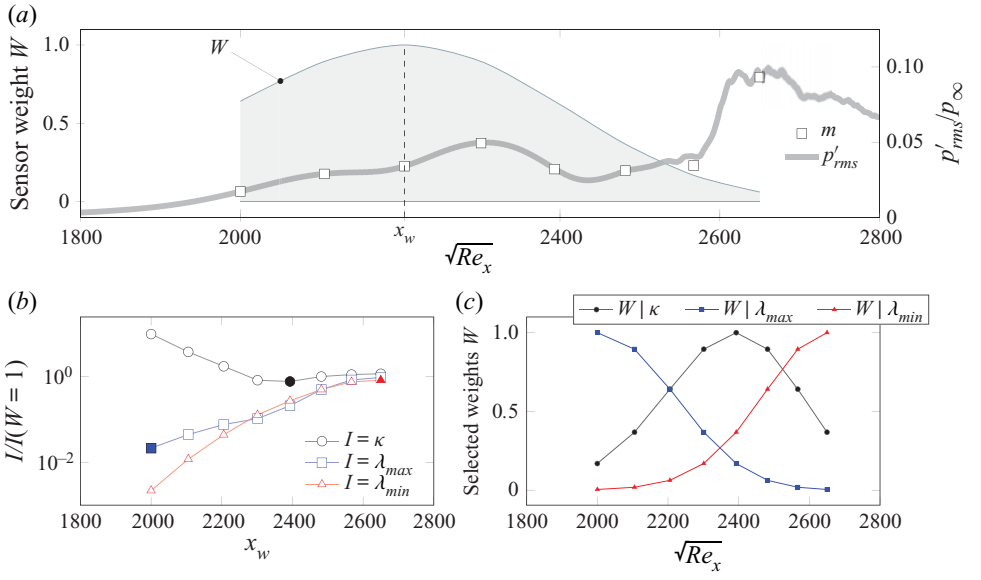


Figure 12. (*a*) Example of streamwise Gaussian weighting. (*b*) For each streamwise placement of the Gaussian weighting, $x_w = x_i$ for $i = \{1, 2, \ldots, 8\}$, the κ, λ_{max} and λ_{min} of $\mathcal{H}$ are reported, normalized by their values for uniform weighting. Shaded symbols mark the optimal value for each criterion, and panel (*c*) shows the corresponding weighting.

Although the expense of the DNS prohibits directly visualizing how the weighting affects the cost landscape, Appendix C discusses a model Lorenz system where the landscape of $\mathcal{J}$ is explicitly computed and the impact of various weighting strategies of observations are evaluated. Guided by those tests, we here examine weighting of wall-pressure observations based on their streamwise position as illustrated in figure 12; spanwise-adjacent observations remain equally weighted since z is a statistically homogeneous direction. We select a weighting function,

$$W(x) = \exp\left[\frac{-(x - x_w)^2}{\sigma_w^2}\right], \tag{5.1}$$

where x_w emphasizes a particular observation station and σ_w determines the influence of neighbouring sensors. The weighting (5.1) is embedded in the EnVar framework using a diagonal matrix $\boldsymbol{W}_s$ of size $N_d \times N_d$, where $N_d = N_t N_x^s N_z^s$ with elements $w_{l,l} = W(\boldsymbol{x}_{i,j}^s)$, where $l = n + (i-1)N_t + (i-1)(j-1)N_t N_x^s$ and $n \in [1, N_t]$, $i \in [1, N_x^s]$ and $j \in [1, N_z^s]$. The cost function, optimal weights and Hessian are revised to

$$\breve{\mathcal{J}} = \tfrac{1}{2}\left\|\boldsymbol{W}_s\boldsymbol{m} - \boldsymbol{W}_s\mathcal{M}\left(\boldsymbol{c}_i\right) - \boldsymbol{W}_s\boldsymbol{H}\boldsymbol{w}\right\|^2_{\boldsymbol{\Sigma}_m^{-1}} + \tfrac{1}{2}\left\|\boldsymbol{P}\boldsymbol{w}\right\|^2_{\boldsymbol{\Sigma}_c^{-1}}, \tag{5.2}$$

$$\breve{\boldsymbol{w}} = -\left(\boldsymbol{H}^{\mathrm{T}}\boldsymbol{W}_s^{\mathrm{T}}\boldsymbol{\Sigma}_m^{-1}\boldsymbol{W}_s\boldsymbol{H} + \boldsymbol{P}^{\mathrm{T}}\boldsymbol{\Sigma}_c^{-1}\boldsymbol{P}\right)^{-1}\left(\boldsymbol{H}^{\mathrm{T}}\boldsymbol{W}_s^{\mathrm{T}}\boldsymbol{\Sigma}_m^{-1}\left\{\boldsymbol{W}_s\mathcal{M}\left(\boldsymbol{c}_i\right) - \boldsymbol{W}_s\boldsymbol{m}\right\}\right) \tag{5.3}$$

and

$$\breve{\mathcal{H}} = \left(\boldsymbol{H}^{\mathrm{T}}\boldsymbol{W}_s^{\mathrm{T}}\boldsymbol{\Sigma}_m^{-1}\boldsymbol{W}_s\boldsymbol{H} + \boldsymbol{P}^{\mathrm{T}}\boldsymbol{\Sigma}_c^{-1}\boldsymbol{P}\right), \tag{5.4}$$

where $(\breve{})$ indicates the influence of weighting $\boldsymbol{W}_s$.

https://doi.org/10.1017/jfm.2021.172 Published online by Cambridge University Press

In practice, starting with members of the first ensemble, which are distributed about the PSE estimate $\boldsymbol{c}_0$, their evolutions are computed using DNS. The associated observation matrix was evaluated, and the Hessian $\mathcal{H}$ was constructed using various weighting strategies. The optimal weight matrix $\boldsymbol{W}_s$ that was identified based on the initial ensemble was adopted for all subsequent EnVar iterations ($i > 0$). Dynamic updates to $\boldsymbol{W}_s$ as the observation and prior terms of the Hessian evolve during the nonlinear optimization is ongoing research, and may further benefit navigating the landscape of $\mathcal{J}$.

The influence of the weighting on the eigenspectrum of the Hessian $\mathcal{H}$ is reported in figure 12(*b*). As one may expect, favourably weighting upstream sensors relative to those in the turbulent region reduces λ_{max}, or largest curvature, of $\mathcal{H}$. Similar to the simple transitional Lorenz model tested in detail in Appendix C, K- and E-optimality for observing the wall pressure in transitional boundary layers yield weightings that favour downstream sensors; these two approaches do not improve convergence of the state estimation algorithm because favouring sensors in chaotic regions create highly oscillatory cost functionals. Due to the computational expense of DNS within each EnVar iteration, we only consider the weighting that reduced λ_{max}, because the associated reduction in extreme curvature of the cost function correlated with improved performance in the Lorenz system.

The adjustments to the $\mathcal{H}$ not only impact the shape of the cost, but they also influence the subsequent distribution of ensemble members, which in turn affects convergence. For example, large curvature would require that ensemble members be sampled closer together in order to accurately approximate the local cost landscape; such tight distribution of members implies higher confidence in an uncertain control vector. Wilson *et al.* (2014) made use of this last point by choosing experimental trajectories which maximize λ_{min}; the minimum curvature in the $\mathcal{H}$ increased and the largest uncertainty of the control vector was reduced since $\boldsymbol{\Sigma}_{\boldsymbol{c}} \propto \mathcal{H}^{-1}$. However, the effect of chaotic behaviour was not an apparent threat in their optimization. For the present transitional boundary-layer configuration, chaos has an excessive impact on local curvature through $\mathcal{H}$, hindering optimization, which led us to consider the alternative approach of weighing sensor data which minimize λ_{max}. In addition to smoothing part of the cost landscape, the approach avoids generating an extremely tight distribution of ensemble members that would undesirably hamper exploration of the cost landscape.

The EnVar estimation procedure was repeated with the observations weighted using the matrix $\boldsymbol{W}_s$ that minimizes λ_{max} (see figure 12*c*). The 2-norm (square root of the maximum eigenvalue) of the control-vector covariance matrix is reported in figure 13(*a*), normalized by its initial value in the EnVar iterations; this quantity is a proxy for the cost function curvature because the control-vector covariance is proportional to $\mathcal{H}^{-1}$. The trend confirms that a weighting strategy that favours upstream observations guards against extreme curvature in $\mathcal{H}$ which would lead to an excessive reduction of $\boldsymbol{\Sigma}_{\boldsymbol{c}}$. Uniform weighting, on the other hand, shrinks $\boldsymbol{\Sigma}_{\boldsymbol{c}}$ by over three orders of magnitude and, hence, $\mathcal{J}$ is dominated by the prior $\boldsymbol{c}$ term and the observations $\boldsymbol{m}$ are relatively ignored which stalls convergence. A closer look at the optimal weighting is provided in figure 13(*b*) where we report the normalized variance of the amplitude of each inflow mode, $\sigma_{f,m}/c_{f,m}$ (%), overlaid on the spectra. The results demonstrate smaller variance in the true inflow modes $\{(100, 0), (110, 0), (40, 1)\}$ since their amplitudes impact the observations and, hence, the cost function. In contrast, larger variances in modes $\{(70, 1), (100, 2), (110, 2)\}$, which are not part of the true inflow condition, signal the lack of trust in those predictions. As discussed in connection with figure 11, our observations are insensitive to those modes and, hence, their uncertainty does not appreciably change the cost function nor does it impact the transition mechanism.

https://doi.org/10.1017/jfm.2021.172 Published online by Cambridge University Press

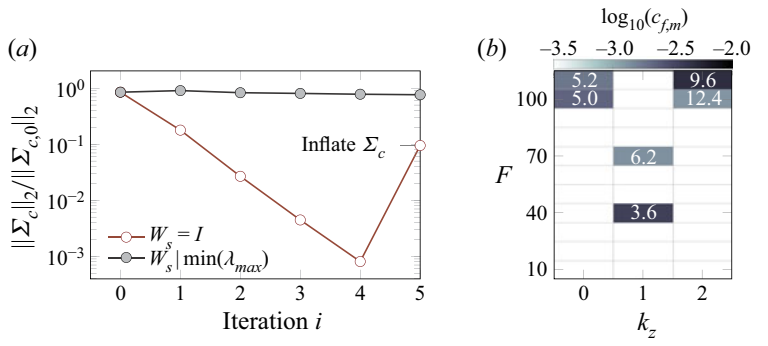


Figure 13. (*a*) Progression of the 2-norm of Σ_c with EnVar iteration, $i \leq 5$ and (*b*) amplitude of key modes. Marked values in (*b*) are the relative uncertainty $(\sigma_{f,m}/c_{f,m}, \sigma_{f,m}/\pi) \times 100$ for the amplitude and phases.

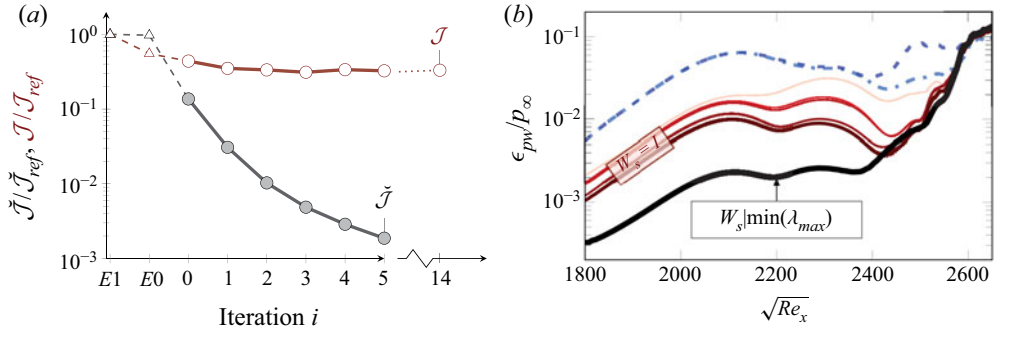


Figure 14. (*a*) Comparison of the normalized cost function when observations are weighted to minimize the maximum eigenvalue of $\mathcal{H}$ vs uniform weighting. (*b*) Reduction of error in the wall pressure when observations are weighted (thick), relative to the uniform weighting results (thin lines reproduced from figure 8).

The behaviour of the cost function with EnVar iterations is reported in figure 14(*a*), and shows two orders of magnitude better reduction than uniform sensor weighting. Cases $E0$ and $E1$ have approximately the same cost because the streamwise weighting reduces to $W \leq 0.17$ for $\sqrt{Re_x} \geq 2400$ (figure 12*c*), which is approximately the point where those flows either transition or remain laminar (see figure 4*a*). Since error reduction in upstream sensors may not necessarily translate to a better overall prediction, we examine the error in the wall pressure as a function of downstream distance in figure 14(*b*). The results show that accuracy is enhanced all the way upstream to the inflow and downstream to the onset of turbulence near $\sqrt{Re_x} \approx 2400$.

Furthermore, the weighting of observations so as to minimize the maximum eigenvalue yields a better estimation of the inflow amplitudes and relative phases. Figure 11(*a*) quantified the error for uniform weighting $(\epsilon_A, \epsilon_\phi) = (19\,\%, 11\,\%)$, $(8\,\%, 6\,\%)$ and $(27\,\%, 1\,\%)$ in predictions of the true modes $(F, k_z) = (100, 0)$, $(110, 0)$ and $(40, 1)$, respectively. The new results with weighted observations reduce these errors to $(\epsilon_A, \epsilon_\phi) = (1\,\%, 3\,\%)$, $(7\,\%, 3\,\%)$ and $(22\,\%, 0.9\,\%)$. The remaining discrepancies relative to the true inflow do not manifest in the sensor data. Most importantly, despite the difference between the estimated and true inflow, the downstream evolution of the two sets of modal amplitudes track one another downstream and the EnVar prediction captures the waves spawned by nonlinearity in the true flow. Figure 15(*a*) shows the development of a streamwise velocity from the EnVar-predicted inflow with the weighted sensor signals,

https://doi.org/10.1017/jfm.2021.172 Published online by Cambridge University Press

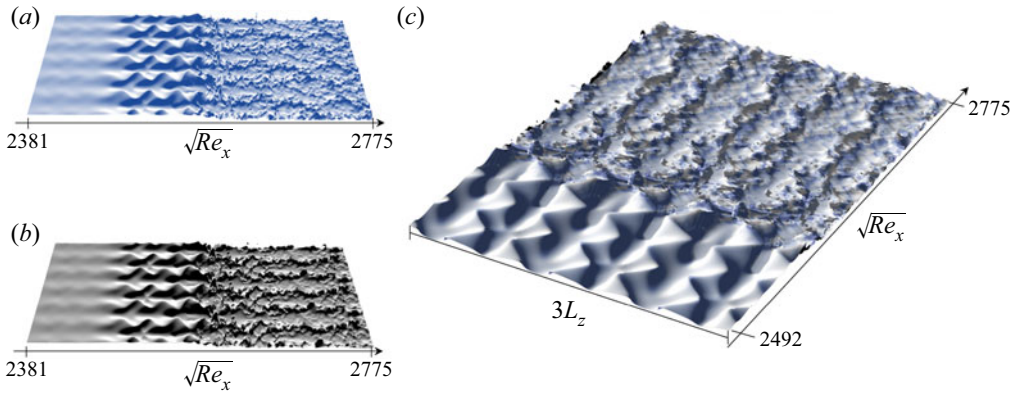


Figure 15. Isosurface of instantaneous streamwise velocity $u = 0.58$ at the end of the observation time horizon $t = T_a$, from (a) favourably weighted EnVar optimization ($i = 5$) and (b) the true state. In (c) the two isosurfaces are overlaid.

compared with the truth in panel (b), and then overlaid together in (c). Transition is accurately captured, both in terms of its onset location and mechanism.

6. Discussion and conclusions

An ensemble variational (EnVar) state estimation algorithm was described for infusing sensor data, or observations, in simulations of high-speed flows. The presentation was focused on transitional boundary layers, and the ability to interpret scarce observations such as wall-pressure data at discrete sensors; however, the methodology is general and applicable with any available observations and forward model. We sought to predict the inflow instability waves that reproduce the sensor data and, in doing so, predict the full flow state encoded in these observations. The first estimate of the unknown inflow condition was obtained using the linear parabolized stability equations, which is an effective approach when sensors are placed in regions where the perturbations dynamics are linear. In flight, the transition location is unknown due to the uncertainty in the energy of environmental disturbances and their interactions. Depending on the placement of sensors, they may be exclusively exposed to turbulence, which would violate PSE assumptions. Therefore, subsequent iterations of the EnVar algorithm are performed using DNS, although any forward nonlinear model that accurately captures the relevant physics can be adopted; where the physics themselves are uncertain or when low-fidelity flow models are used, we caution that the impact of model inadequacies must be considered.

The EnVar algorithm was adopted for the interpretation of wall-pressure observations at sixty-four sensing locations from a $M = 4.5$ flat-plate transitional boundary layer. The sensors spanned the linear, nonlinear and chaotic flow regimes. And the estimated flow successfully identified an inflow spectra that yielded accurate predictions of the wall pressure, transition location and the transition mechanism. However, the reduction of the cost function was not sufficiently satisfactory, even with inflation of the ensemble covariance.

Favourably weighting upstream observations reduces the maximum eigenvalue of the Hessian of the cost function and, hence, the most extreme curvature of the cost function. The outcome is improved convergence of the EnVar algorithm, in particular, a more accurate prediction of the inflow disturbances and, hence, the flow. This sensor

https://doi.org/10.1017/jfm.2021.172 Published online by Cambridge University Press

weighting is counter to traditional strategies that attempt to minimize the condition number of the Hessian in order to ensure its accurate inversion, and to strategies that increase the Hessian minimum eigenvalue to improve trust in the predicted minimum. The best weighting strategy is different precisely because of the present configuration which involves transition to chaotic flow. The underlying cost functional landscape is tortuous and oscillatory, which hampers the optimization and leads to narrow search regions. Our weighting approach lessens that difficulty, and leads to better convergence of the algorithm. Note that we achieve this goal without flattening the cost functional in all parameter directions, which would also be undesirable because an entirely flat cost functional would lead to significant prediction uncertainties. Future efforts should quantify the degree to which errors in observations impair their accurate interpretation, apply the framework to experimental data, and explore the optimal measurement modality and sensor weighting and placement.

Acknowledgements. The authors are grateful to Professor J. Larsson for sharing the Hybrid code.

Funding. The authors acknowledge the financial support from the US Air Force Office of Scientific Research (grant number FA9550-19-1-0230) and the Office of Naval Research (grant number N00014-17-1-2339). Computational resources were provided by the Maryland Advanced Research Computing Center (MARCC).

Declaration of interests. The authors report no conflict of interest.

Author ORCIDs.
David A. Buchta https://orcid.org/0000-0002-7068-6226;
Tamer A. Zaki https://orcid.org/0000-0002-1979-7748.

Appendix A. EnVar gradient accuracy

The purpose of this appendix is to compare the gradient of the cost functional evaluated using EnVar to two finite-difference approximations, the first using the quadratic form of the cost functional $\tilde{\mathcal{J}}$ and the second using the full nonlinear form $\mathcal{J}$. As in similar assessments of gradient accuracy (Vishnampet *et al.* 2015; Buchta *et al.* 2016), we consider the Taylor series expansion of the quadratic cost function which is exact,

$$\tilde{\mathcal{J}}(\boldsymbol{w}) = \tilde{\mathcal{J}}(0) + \frac{\partial \tilde{\mathcal{J}}}{\partial \boldsymbol{w}}^{\mathrm{T}} \boldsymbol{w} + \frac{1}{2}\boldsymbol{w}^{\mathrm{T}} \frac{\partial^2 \tilde{\mathcal{J}}}{\partial \boldsymbol{w}^2}\boldsymbol{w}. \tag{A1}$$

Consider the weights in the EnVar gradient direction,

$$\boldsymbol{w} = -\alpha \frac{\partial^2 \tilde{\mathcal{J}}}{\partial \boldsymbol{w}^2}^{-1} \frac{\partial \tilde{\mathcal{J}}}{\partial \boldsymbol{w}}, \tag{A2}$$

substitute in (A1), and rearranging yields an error measure,

$$\epsilon_p \equiv \left| \underbrace{\frac{\tilde{\mathcal{J}}(\boldsymbol{w}) - \tilde{\mathcal{J}}(0)}{\alpha} + \frac{\partial \tilde{\mathcal{J}}}{\partial \boldsymbol{w}}^{\mathrm{T}} \frac{\partial^2 \tilde{\mathcal{J}}}{\partial \boldsymbol{w}^2}^{-1} \frac{\partial \tilde{\mathcal{J}}}{\partial \boldsymbol{w}}}_{\epsilon_1} - \frac{\alpha}{2} \frac{\partial \tilde{\mathcal{J}}}{\partial \boldsymbol{w}}^{\mathrm{T}} \frac{\partial^2 \tilde{\mathcal{J}}}{\partial \boldsymbol{w}^2}^{-1} \frac{\partial \tilde{\mathcal{J}}}{\partial \boldsymbol{w}} \right|. \tag{A3}$$

Equation (A3) should be identically zero. Any errors in ϵ_p are due to machine round off, which will increase as we reduce α. In addition, ϵ_1 is the error in approximating the derivative of a quadratic function, which is exact in EnVar, by a first-order finite-difference approximation. This error will reduce with α until it is dominated by finite-precision effects. Figure 16 reports both errors, ϵ_p (light curve) and ϵ_1 (dark curve).

https://doi.org/10.1017/jfm.2021.172 Published online by Cambridge University Press

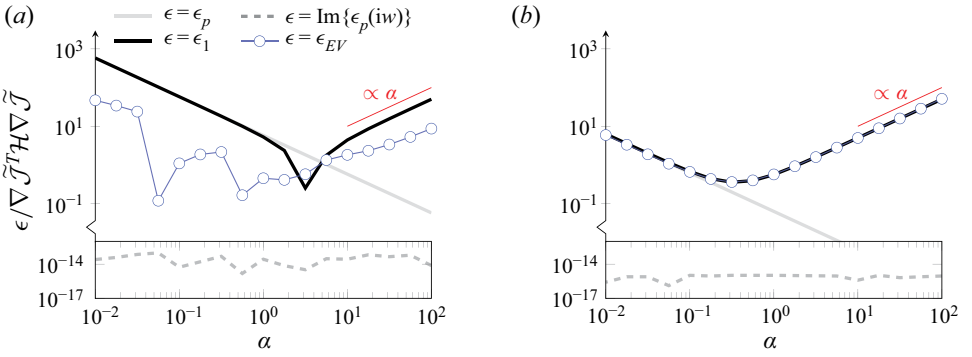


Figure 16. Accuracy of the cost-functional gradient computed using the EnVar approach in the transitional boundary layer. (*a*) Uniform weighting of observations $\boldsymbol{W}_s = \boldsymbol{I}$ (EnVar iteration $i = 14$); (*b*) weighted observations $\boldsymbol{W}_s \mid \lambda_{max}$ (iteration $i = 5$).

As anticipated, the ϵ_p is only susceptible to finite precision. This assertion is further confirmed by re-computing ϵ_p using a complex step $\boldsymbol{w} \rightarrow \mathrm{i}\boldsymbol{w}$ in (A3). The imaginary part of the error yields

$$\mathrm{Im}\left\{\epsilon_p(\mathrm{i}\boldsymbol{w})\right\} = \left|\mathrm{Im}\left(\frac{\tilde{\mathcal{J}}(\mathrm{i}\boldsymbol{w})}{\alpha}\right) + \frac{\partial \tilde{\mathcal{J}}}{\partial \boldsymbol{w}}^{\mathrm{T}} \frac{\partial^2 \tilde{\mathcal{J}}}{\partial \boldsymbol{w}^2}^{-1} \frac{\partial \tilde{\mathcal{J}}}{\partial \boldsymbol{w}}\right| = 0, \tag{A4}$$

which bypasses the effect of differencing in (A3). As a result, the errors which are reported in figure 16 (dashed curve) decrease to insignificant values.

The above approaches verify the gradient implementation for a quadratic cost functional, $\tilde{\mathcal{J}}$. For a cost function that is not strictly quadratic $\mathcal{J}$, its local tangent direction may not correspond with the EnVar-based gradient. The deviation is evaluated by comparing a finite-difference approximation of the gradient to an EnVar approximation,

$$\epsilon_{EV} = \left|\frac{\boxed{\mathcal{J}(\boldsymbol{w})} - \tilde{\mathcal{J}}(0)}{\alpha} + \frac{\partial \tilde{\mathcal{J}}}{\partial \boldsymbol{w}}^{\mathrm{T}} \frac{\partial^2 \tilde{\mathcal{J}}}{\partial \boldsymbol{w}^2}^{-1} \frac{\partial \tilde{\mathcal{J}}}{\partial \boldsymbol{w}}\right|. \tag{A5}$$

The gradient accuracy is reported in figure 16 for two cases: (*a*) when the sensors are equally weighted and (*b*) when the upstream ones are favoured. In the former case, the degree of accuracy is affected by nonlinearity of the forward system. We find that the EnVar approximation is suitable for an appropriate choice of the step size. The results further verify that the EnVar gradient approximation is accurate, and it improves for favourable observation weighting.

Appendix B. Estimate of control-vector covariance

In this appendix we motivate the relationship between the Hessian of $\tilde{\mathcal{J}}$ and the control-vector covariance matrix $\boldsymbol{\Sigma_c}$ which is used to generate ensemble members. We consider a stationary point $\nabla_w \tilde{\mathcal{J}} = 0$, and evaluate the total variation of the cost-function gradient,

$$\delta\left(\frac{\partial \tilde{\mathcal{J}}}{\partial \boldsymbol{w}}\right) = \frac{\partial^2 \tilde{\mathcal{J}}}{\partial \boldsymbol{w}^2}\delta\boldsymbol{w} + \frac{\partial^2 \tilde{\mathcal{J}}}{\partial \boldsymbol{m}\partial \boldsymbol{w}}\delta\boldsymbol{m} = 0. \tag{B1}$$

https://doi.org/10.1017/jfm.2021.172 Published online by Cambridge University Press

The variation of the weights due to perturbations in observations is therefore

$$\delta \boldsymbol{w} = -\frac{\partial^2 \tilde{\mathcal{J}}}{\partial \boldsymbol{w}^2}^{-1} \frac{\partial^2 \tilde{\mathcal{J}}}{\partial \boldsymbol{m} \partial \boldsymbol{w}} \delta \boldsymbol{m}, \tag{B2}$$

where the second derivatives can be evaluated from the quadratic cost function (2.9),

$$\frac{\partial^2 \tilde{\mathcal{J}}}{\partial \boldsymbol{w}^2} = \boldsymbol{H}^{\mathrm{T}} \boldsymbol{\Sigma}_{\boldsymbol{m}}^{-1} \boldsymbol{H} + \boldsymbol{P}^{\mathrm{T}} \boldsymbol{\Sigma}_{\boldsymbol{c}}^{-1} \boldsymbol{P} \quad \text{and} \quad \frac{\partial^2 \tilde{\mathcal{J}}}{\partial \boldsymbol{m} \partial \boldsymbol{w}} = -\boldsymbol{H}^{\mathrm{T}} \boldsymbol{\Sigma}_{\boldsymbol{m}}^{-1}. \tag{B3a,b}$$

Then, the covariance of weights is

$$\mathbb{E}\left[\delta \boldsymbol{w} \delta \boldsymbol{w}^{\mathrm{T}}\right] = \mathbb{E}\left[\left(\boldsymbol{H}^{\mathrm{T}} \boldsymbol{\Sigma}_{\boldsymbol{m}}^{-1} \boldsymbol{H} + \boldsymbol{P}^{\mathrm{T}} \boldsymbol{\Sigma}_{\boldsymbol{c}}^{-1} \boldsymbol{P}\right)^{-1} \boldsymbol{H}^{\mathrm{T}} \boldsymbol{\Sigma}_{\boldsymbol{m}}^{-1} \boldsymbol{H} \left(\boldsymbol{H}^{\mathrm{T}} \boldsymbol{\Sigma}_{\boldsymbol{m}}^{-1} \boldsymbol{H} + \boldsymbol{P}^{\mathrm{T}} \boldsymbol{\Sigma}_{\boldsymbol{c}}^{-1} \boldsymbol{P}\right)^{-1}\right], \tag{B4}$$

which can be simplified to

$$\underbrace{\mathbb{E}\left[\delta \boldsymbol{w} \delta \boldsymbol{w}^{\mathrm{T}}\right]}_{\boldsymbol{\Sigma}_{\boldsymbol{w}}} \approx \left(\underbrace{\boldsymbol{H}^{\mathrm{T}} \boldsymbol{\Sigma}_{\boldsymbol{m}}^{-1} \boldsymbol{H} + \boldsymbol{P}^{\mathrm{T}} \boldsymbol{\Sigma}_{\boldsymbol{c}}^{-1} \boldsymbol{P}}_{\mathcal{H}}\right)^{-1}. \tag{B5}$$

The left-hand side of (B5) is the covariance of weights and the right-hand side is the inverse Hessian of $\tilde{\mathcal{J}}$. This approximation holds for $\left\|(\boldsymbol{H}^{\mathrm{T}} \boldsymbol{\Sigma}_{\boldsymbol{m}}^{-1} \boldsymbol{H})^{-1} (\boldsymbol{P}^{\mathrm{T}} \boldsymbol{\Sigma}_{\boldsymbol{c}}^{-1} \boldsymbol{P})\right\| \ll \|\boldsymbol{I}\|$, which is not immediately clear by inspection of (B4). However, we clarify the simplification of (B4) to (B5) by recognizing that the right-hand side of (B4) has the form $(\boldsymbol{A}+\boldsymbol{B})^{-1}\boldsymbol{A}(\boldsymbol{A}+\boldsymbol{B})^{-1}$, where $\boldsymbol{A}$ and $\boldsymbol{B}$ are same-sized invertible matrices. The expression is simplified in the following steps:

$$\begin{aligned}
(\boldsymbol{A}+\boldsymbol{B})^{-1}\boldsymbol{A}(\boldsymbol{A}+\boldsymbol{B})^{-1} &= (\boldsymbol{I}+\boldsymbol{A}^{-1}\boldsymbol{B})^{-1}\boldsymbol{A}^{-1}\boldsymbol{A}(\boldsymbol{I}+\boldsymbol{A}^{-1}\boldsymbol{B})^{-1}\boldsymbol{A}^{-1} \\
&= \left[\boldsymbol{A}(\boldsymbol{I}+\boldsymbol{A}^{-1}\boldsymbol{B})(\boldsymbol{I}+\boldsymbol{A}^{-1}\boldsymbol{B})\right]^{-1} \\
&= \left[(\boldsymbol{A}+\boldsymbol{B})(\boldsymbol{I}+\boldsymbol{A}^{-1}\boldsymbol{B})\right]^{-1} \\
&\approx (\boldsymbol{A}+\boldsymbol{B})^{-1}
\end{aligned} \tag{B6}$$

provided $\left\|\boldsymbol{A}^{-1}\boldsymbol{B}\right\| \ll \|\boldsymbol{I}\|$.

Next, we show the relationship between the covariance of the weights and the control-vector covariance matrix. By its definition, the estimate of the control vector is a weighted superposition of perturbations to the prior and, hence, its variation is $\delta \boldsymbol{c} = \boldsymbol{P}\delta \boldsymbol{w}$. Then, the control-vector covariance matrix is

$$\begin{aligned}
\underbrace{\mathbb{E}\left[\delta \boldsymbol{c} \delta \boldsymbol{c}^{\mathrm{T}}\right]}_{\boldsymbol{\Sigma}_{\boldsymbol{c}}^{\star}} &= \boldsymbol{P}\mathbb{E}\left[\delta \boldsymbol{w} \delta \boldsymbol{w}^{\mathrm{T}}\right]\boldsymbol{P}^{\mathrm{T}} \\
&\approx \boldsymbol{P}\mathcal{H}^{-1}\boldsymbol{P}^{\mathrm{T}},
\end{aligned} \tag{B7}$$

using (B5). By updating the ensemble members using $\boldsymbol{P}_{i+1} = \sqrt{N-1}\boldsymbol{P}_i\mathcal{H}^{-1/2}\boldsymbol{U}$, where $\boldsymbol{U}$ is a random, mean preserving, unitary matrix, we guarantee that the control-vector covariance matrix, $\boldsymbol{\Sigma}_{\boldsymbol{c}}^{i+1} = 1/(N-1)\boldsymbol{P}_{i+1}\boldsymbol{P}_{i+1}{}^{\mathrm{T}}$, adheres to the relationship (B7).

https://doi.org/10.1017/jfm.2021.172 Published online by Cambridge University Press

Appendix C. Observation-infused simulations of Lorenz system

In this appendix we use a low-dimensional chaotic system to (i) probe performance of the EnVar technique described in § 2 and to (ii) contrast different sensor-weighting techniques. The system models thermal convection in a two-dimensional domain that is periodic in the streamwise direction and forced by gravity (g) and a temperature difference between the upper and lower boundaries, $\Delta T = T(0) - T(H)$. The fluid is ideal with thermal diffusivity $k = \kappa/\rho c_p$, kinematic viscosity ν and coefficient of thermal expansion α. The low-dimensional dynamics (Saltzman 1962; Lorenz 1963) consider the temperature fluctuations (T') and velocity potential ψ in Fourier space,

$$T'(x, y, t) \propto Y(t)\sqrt{2}\cos\left(\tfrac{1}{2}k_a x\right)\sin\left(\tfrac{1}{2}k_y y\right) - Z(t)\sin\left(k_y y\right), \tag{C1}$$

$$\psi(x, y, t) \propto X(t)\sqrt{2}\sin\left(\tfrac{1}{2}k_a x\right)\sin\left(\tfrac{1}{2}k_y y\right), \tag{C2}$$

where $k_a = a2\pi/H$ and $k_y = 2\pi/H$ are the streamwise and wall-normal wavenumbers. The time dependent Fourier coefficients $\boldsymbol{X} = [X, Y, Z]^T$ are solutions to

$$\frac{\mathrm{d}X}{\mathrm{d}t} = \sigma(Y - X), \quad \frac{\mathrm{d}Y}{\mathrm{d}t} = -XZ + \rho X - Y \quad \text{and} \quad \frac{\mathrm{d}Z}{\mathrm{d}t} = XY - \beta Z, \tag{C3a–c}$$

with initial perturbation to the system $[X, Y, Z](t = 0) = [X_o, Y_o, Z_o]$. The specific configuration we consider follows Saltzman (1962): $a = \sqrt{1/2}$, $\sigma = 10$, $\rho = 28$, $\beta = 8/3$ and $\boldsymbol{X}_o = [0, 1, 0]^{\mathrm{T}}$.

Figure 17(a) shows transition to chaos. The initial disturbance is comprised only of temperature fluctuations, which subsequently amplify and generate velocity perturbations. Due to ΔT, cold fluid cools further and conversely hot heats up, amplifying the instability by $t \approx 0.4$. With gravity, the convection cells overturn. The cells oscillate about a new equilibrium state, which amplifies and overturns again by $t > 15$. Beyond this time, the behaviour is chaotic. The trajectory of the state $\boldsymbol{X}$ is shown in figure 17(b), and the observed quantity, Y, is shown in (c). The behaviour in figure 17(c) is similar to boundary-layer transition: amplification about an equilibrium (laminar) state and transition to chaos (turbulence).

Of the three state variables, we observe part of Y. We then attempt to (i) identify the complete initial state $\boldsymbol{X}_o$ that (ii) reproduces observations, and (iii) reconstruct the solution trajectory beyond the observed horizon. Specifically, the observation vector is given by $\boldsymbol{m} = [Y(5), Y(6), \ldots, Y(t_f)]^{\mathrm{T}}$ to time $t_f = 20$. The choice was motivated by the transitional boundary layer (figure 3c) where observations are available downstream of the inflow and across the nonlinear and chaotic regimes. The control vector we seek to identify is $\boldsymbol{c} = [X_o, Y_o, Z_o]^{\mathrm{T}}$. Since the observations $\boldsymbol{m}$, early on ($t < 15$), oscillate near $Y = -6\sqrt{2}$ in figure 17(c), we consider the initial perturbation originated near equilibrium point, $\boldsymbol{c}_0 = [-6\sqrt{2}, -6\sqrt{2}, 27]^{\mathrm{T}}$. The system (C3$a$–$c$) is integrated using a standard fourth-order Runge–Kutta method and discretized with a fixed time step $\Delta t = 0.01$, which is the same numerical method that generated $\boldsymbol{m}$. The parameter and observation covariance matrices used in the EnVar method are respectively set to $\Sigma_{\boldsymbol{c}} = \sigma_c \mathrm{I}$ and $\Sigma_{\boldsymbol{m}} = \sigma_m \mathrm{I}$, where $\sigma_c = 1$ and $\sigma_m = 10^{-3}$.

Results from the EnVar initial-state estimation are reported in figure 18, where two time horizons of observations are contrasted. For each case, one hundred iterations were performed. When the time horizon includes observations within the chaotic regime (figure 18a), the predictions are qualitatively similar to the results for the transitional boundary layer: the time of transition in the thermal system near $t \approx 15$ appears

https://doi.org/10.1017/jfm.2021.172 Published online by Cambridge University Press

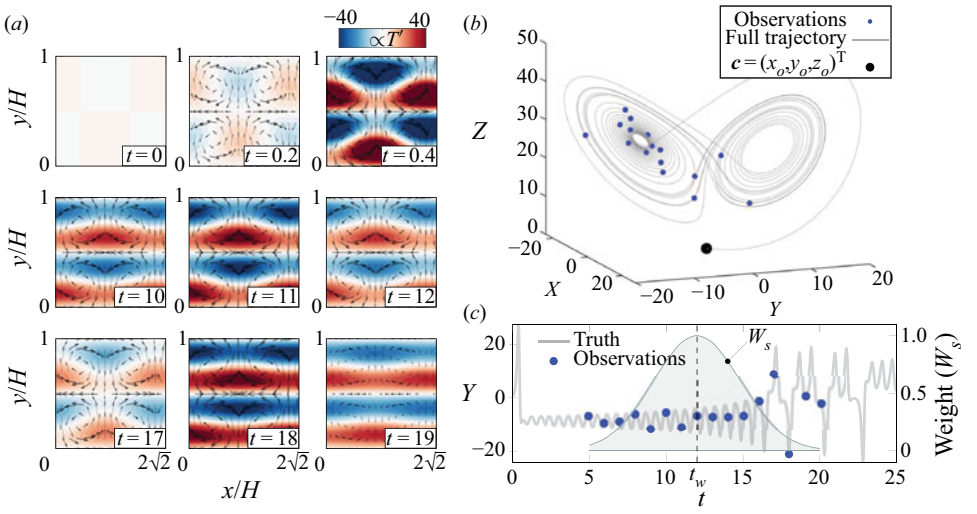


Figure 17. (*a*) Instantaneous temperature (colour) and velocity (arrows). (*b*) True phase-space trajectory (thick grey), observation locations (small symbols) and initial condition (large symbol). (*c*) Time evolution of Y: observations (symbols), truth (thick grey) and Gaussian weighting strategy (blue/grey).

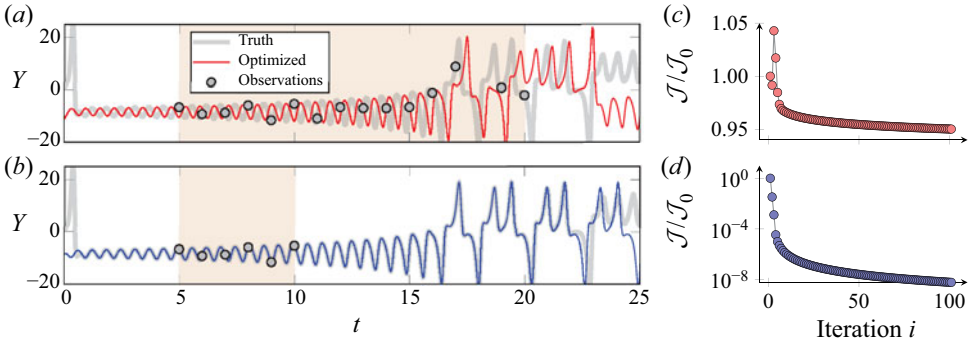


Figure 18. (*a*,*b*) The estimated time evolution of Y after one hundred EnVar iterations. Shaded intervals identify the extents of the observation time horizons, $\boldsymbol{m} = [Y(5), Y(6), \ldots, Y(t_f)]^{\mathrm{T}}$. (*a*) Target observation horizon $t_f = 20$; (*b*) shorter test horizon $t_f = 10$. (*c*,*d*) Convergence history of the normalized cost function.

to be captured, and a very modest reduction in cost is achieved in figure 18(*c*). When only the first five observations are considered (figure 18*b*), the estimated initial condition reproduces the measurements with higher accuracy and predicts the evolution for a longer duration. In both cases, it is important to note that the predicted state deviates from the true initial condition. In addition, while disregarding sensor data in the second case may appear *ad hoc*, this test indicates (i) that earlier acquisition provides better information about $t = 0$ than later times, (ii) that later observations negatively impact gradient-based optimization, or (iii) that a mixture of these two effects takes place. The first proposition may appear natural, but is not necessarily accurate: small perturbations in X_o or Z_o may be entirely missed by early observations of Y. In the same manner, a wall-pressure sensor near the inflow may be entirely insensitive to an inflow disturbance whose wall signature only develops downstream.

https://doi.org/10.1017/jfm.2021.172 Published online by Cambridge University Press

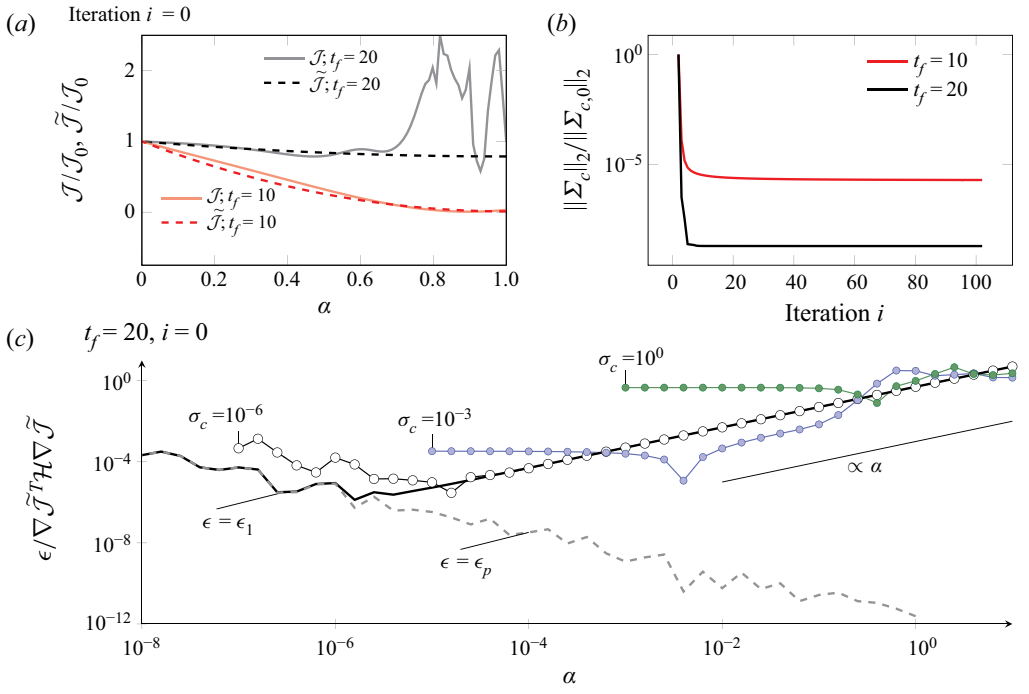


Figure 19. (*a*) Effect of discarding observations on the shape of the cost function, evaluated in the gradient direction, at the initial EnVar iteration. Full observation horizon $t_f = 20$; truncated horizon $t_f = 10$. (*b*) The 2-norm of the covariance matrix of the control vector as a function of EnVar iterations. (*c*) Errors in the gradient of the cost functional evaluated using EnVar vs step size α in the gradient direction. Symbols: errors relative to finite difference ϵ_{EV}, at various levels of ensemble covariance $\Sigma_c = \sigma_c \boldsymbol{I}$. See Appendix A for definitions of ϵ_1 and ϵ_p.

In order to diagnose the convergence of $\mathcal{J}$ in figure 18(*c*,*d*), we probe the following: cost-function shape along the gradient direction, the progress of Σ_c which depends on the Hessian of $\tilde{\mathcal{J}}$ and the gradient accuracy using ((A3)–(A4)). Figure 19(*a*) shows the landscape of $\mathcal{J}(\boldsymbol{w})$ and $\tilde{\mathcal{J}}(\boldsymbol{w})$ as a function of the step size in the gradient direction

$$\boldsymbol{w} = -\alpha \frac{\partial^2 \tilde{\mathcal{J}}}{\partial \boldsymbol{w}^2}^{-1} \frac{\partial \tilde{\mathcal{J}}}{\partial \boldsymbol{w}}, \tag{C4}$$

with $0 \leq \alpha \leq 1$, where $\alpha = 1$ is the optimal step size for a quadratic function. When only early observations are considered, the approximation $\tilde{\mathcal{J}}$ follows more closely $\mathcal{J}$ which appears amenable to gradient-based optimization. However, when later observations are included, $\mathcal{J}$ is oscillatory and its linearization $\tilde{\mathcal{J}}$ is only valid for small distances from the previous estimate of the control vector. Notably in figure 19(*b*), $||\Sigma_c||_2$ is two orders of magnitude smaller in the latter case. As such, subsequent ensemble members will remain close to the prior $\boldsymbol{c}$, the observations $\boldsymbol{m}$ are ignored and the $\mathcal{J}$ remains flat. Figure 19(*c*) shows that the initial gradient is relatively accurate. The first-order gradient accuracy can be improved by constructing ensemble members closer to the mean (e.g. $\sigma_c = 10^{-3}$ and $\sigma_c = 10^{-6}$). However, as the EnVar framework progresses, the posterior statistics of the Hessian reduce uncertainty of the control vector, thereby reducing Σ_c as in figure 19(*b*).

The conclusion from figure 19 is that incorporating later observations, which are chaotic, yields an oscillatory cost functional shape and unpredictable changes in the cost,

https://doi.org/10.1017/jfm.2021.172 Published online by Cambridge University Press

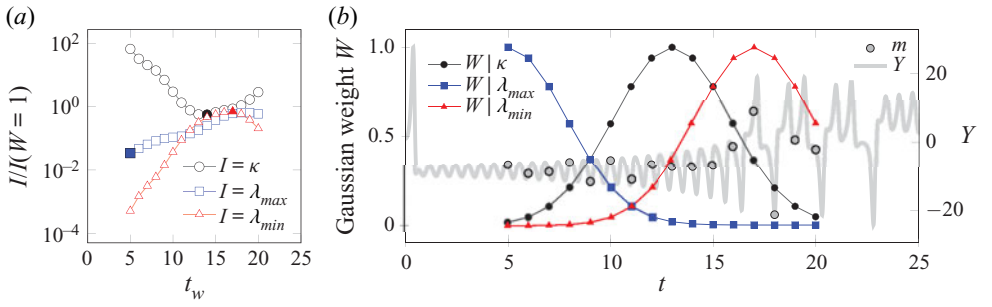


Figure 20. (*a*) For each temporal placement of the Gaussian weighting, $t_w = t_i$ for $i = [5, 6, \ldots, 20]$, the κ, λ_{max} and λ_{min} of $\mathcal{H}$ are reported, normalized by their values for uniform weighting. Shaded symbols mark the optimal value for each criterion, and panel (*b*) shows the corresponding weighting.

even though the gradient near $\alpha = 0$ is well approximated. Cost reduction is subsequently hindered because of extreme reduction in the control-vector covariance due to large sensitivity (large curvature in $\mathcal{H}$) from observations that are very sensitive to the initial condition. While not shown, control-vector covariance inflation alone does not improve the cost reduction when later observations are considered.

Instead of simply eliminating observations, sensor-weighting strategies are evaluated for the Lorenz system. We adopt a weighting function,

$$W = \exp\left[\frac{-(t - t_w)^2}{\sigma_w^2}\right], \tag{C5}$$

which biases a particular observation time t_w, and σ_w controls the influence of neighbouring sensors. The impact of the weights on the performance of the EnVar algorithm can be related to the eigenspectrum behaviour of $\mathcal{H}$, specifically the following. (i) Minimizing the condition number κ promotes its accurate inversion and, hence, accurate evaluation of the ensemble weights. (ii) Maximizing the minimum eigenvalue λ_{min} reduces the largest uncertainty in the estimated control vector (Ucinski 2004; Colburn 2011; Wilson *et al.* 2014). (iii) Minimizing the maximum eigenvalue λ_{max} guards against the most extreme curvature, which we also interpret as the most egregious over-estimate of trust in a component of the control vector. Figure 20(*a*) reports the impact of different t_w on these invariants of $\mathcal{H}$, and figure 20(*b*) shows the Gaussian profile that best accomplishes each strategy. The results demonstrate that κ is minimized by favourably weighting the intermediate observations; maximizing λ_{min} is achieved by favouring later ones; minimizing λ_{max} places the focus on early observations. These trends in the context of chaotic convection apply similarly to transitional boundary layers when observations span the linear, nonlinear and chaotic regimes.

The performance of the EnVar algorithm with the above sensor-weighting strategies is reported in figure 21(*a*). The best reduction of the cost function is achieved by favouring the earlier observations, or minimizing λ_{max}, thus guarding against extreme curvature. This trend is consistent with the earlier test in figure 18(*c*,*d*). The figure also shows that convergence is further accelerated by applying covariance inflation every five iterations. Previous research has proposed amplifying the parameter covariance in order to avoid over-estimating confidence in them (e.g. Anderson & Anderson 1999; Colburn 2011; da Silva & Colonius 2018). In doing so, convergence accelerates by several orders of magnitude more.

https://doi.org/10.1017/jfm.2021.172 Published online by Cambridge University Press

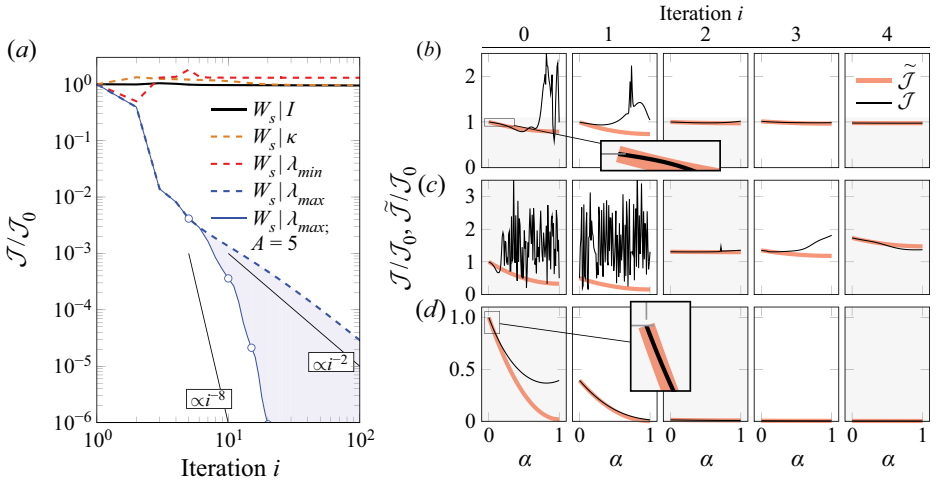


Figure 21. (*a*) Comparison of normalized cost functional during EnVar optimizations that adopt different sensor-weighting ($\boldsymbol{W}_s$) schemes. (*b–d*) Cost functional in the gradient direction vs the step size for the first five iterations. Parameters: (*b*) $\boldsymbol{W}_s = \boldsymbol{I}$; (*c*) $\boldsymbol{W}_s \mid \lambda_{min}$; (*d*) $\boldsymbol{W}_s \mid \lambda_{max}$.

Ultimately, weighting of observations aims to modify the landscape of the cost function. Figure 21(*b–d*) display the landscape during the first five EnVar iterations, using the same approach discussed for figure 19(*a*). Deviation between the thin and thick curves in each panel is due to the linear approximation within $\mathcal{J}$ by $\tilde{\mathcal{J}}$, or precisely full nonlinear observations $\mathcal{M}(\boldsymbol{c} + \boldsymbol{P}\boldsymbol{w})$ (thin) vs the linearized $\mathcal{M}(\boldsymbol{c}) + \boldsymbol{H}\boldsymbol{w}$ (thick). The cost function $\mathcal{J}$ is oscillatory when weighting all observations equally or favouring later ones. Oscillations are most pronounced for the latter case which aims to increase λ_{min}, or reduce the largest control-vector variance – a strategy that is inadequate for a chaotic cost function and where late observations are extremely sensitive to uncertainties. The ability to reduce the cost reduction is severely hampered. Although by $i = 2$ the cost function appears smooth, the control-vector covariance has decreased significantly that all observations are ignored, indiscriminately, and the cost reduction remains approximately zero. In contrast, minimizing λ_{max}, and thus guarding against the largest curvature in $\mathcal{H}$, smoothes the cost function, results in predictable convexity and promotes convergence.

The degree to which nonlinearity affects gradient accuracy is quantified for the progression of EnVar iterations in figure 22. We note that due to the initial sampling of $\boldsymbol{\Sigma}_{\boldsymbol{c}} = \sigma_c \boldsymbol{I}$, the tangent approximation is not exactly obeyed, initially; though biasing earlier sensors in figure 22(*c*) shows improvement. After approximately four EnVar iterations, gradients are accurate and their accuracy is insensitive to weighting, which is due to a decrease in $||\boldsymbol{\Sigma}_{\boldsymbol{c}}||$ (see figure 23*b*) and, hence, a refined local tangent approximation. Even with improved gradient accuracy by $i = 4$, chaotic systems with oscillatory, or wrinkled, cost functions have local minima with large curvatures that tend to over-amplify trust in unknown control-vector parameters; the optimization thus stagnates at $\mathcal{J}/\mathcal{J}_0 \approx 1$ (cf. figure 21*b*,*c*) because it is trapped in a local minimum.

We summarize by showing the final prediction of Y-dynamics in figure 23(*a*); trends for X and Z are similar, and are therefore not shown. The predictions in the figure were obtained using the weighting scheme which minimizes λ_{max}, or extreme curvature of the cost functional, and occasional inflation of the parameters covariance. The prediction matches the truth beyond the time horizon of the observations to $t = 25$. Lorenz (1963)

https://doi.org/10.1017/jfm.2021.172 Published online by Cambridge University Press

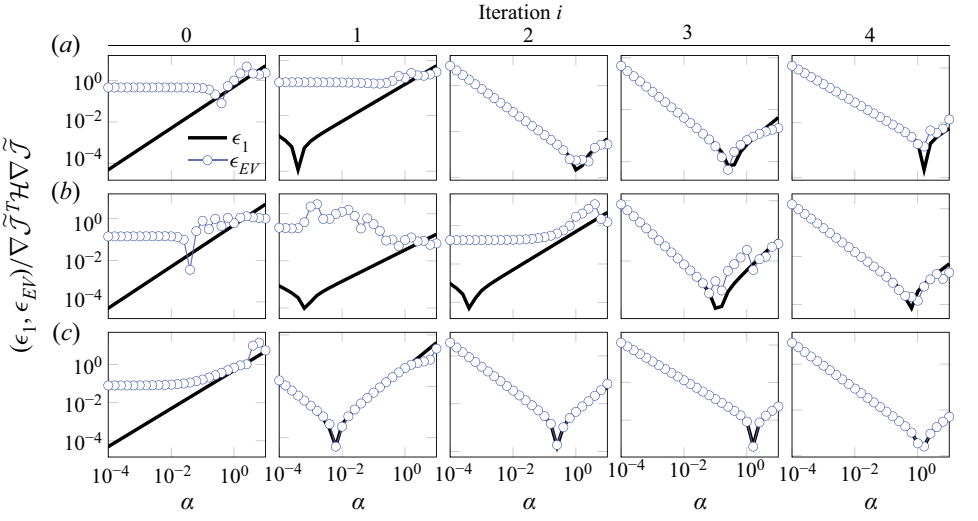


Figure 22. Accuracy of the gradient of the cost function evaluated using EnVar vs the step size in the optimal direction. Results are shown for EnVar iterations $i \leq 4$. Parameters: (*a*) $\boldsymbol{W}_s = \boldsymbol{I}$, (*b*) $\boldsymbol{W}_s|\lambda_{min}$ and (*c*) $\boldsymbol{W}_s|\lambda_{max}$.

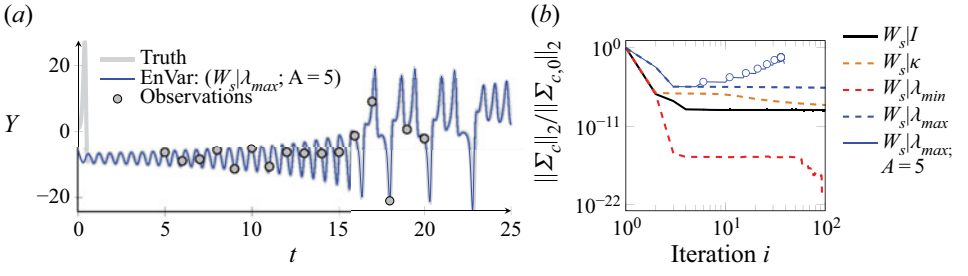


Figure 23. (*a*) The time evolution of Y estimated using EnVar with weighted observations to guard against worst-case Hessian curvature, control-vector covariance inflation every five iterations and stopping criteria $\mathcal{J}/\mathcal{J}_0 \leq 10^{-11}$. (*b*) Normalized 2-norm of the control-vector covariance matrix; symbols mark iterations when covariance inflation is applied.

notes that incomplete and imprecise data acquisition does not guarantee a data match for $t \to \infty$; yet performance is surely enhanced. Notably, the optimized initial condition does not equal the truth, rather $\boldsymbol{X}_o$ was adjusted in a manner to reproduce the $\boldsymbol{X}$ dynamics by $t \approx 1$, which is earlier than the first observation at $t = 5$. Similar behaviour was observed in boundary-layer transition in figure 11(*c*,*d*), which highlights the possibility of identifying local optima relative to the truth. Figure 23(*b*) shows how the recommended weighting avoids over-shrinking of $\boldsymbol{\Sigma_c}$. For uniform weighting, the parameter covariance matrix $\boldsymbol{\Sigma_c}$ shrinks by approximately eight orders of magnitude by the third EnVar iteration, due to sensitivity of observations to small changes in $\boldsymbol{c}$. Without resorting *ad hoc* methods of discarding observation data, weighting based on reducing extreme curvature favours earlier sensors and enhances the outcome of the optimization.

References

Anderson, J.L. & Anderson, S.L. 1999 A Monte Carlo implementation of the nonlinear filtering problem to produce ensemble assimilations and forecasts. *Mon. Weath. Rev.* **127** (12), 2741–2758.

https://doi.org/10.1017/jfm.2021.172 Published online by Cambridge University Press

BALAKUMAR, P. & CHOU, A. 2018 Transition prediction in hypersonic boundary layers using receptivity and freestream spectra. *AIAA J.* **56** (1), 193–208.

BERRIDGE, D.C., KOSTAK, H., MCKIERNAN, G., WHEATON, B.M., WOLF, T.D. & SCHNEIDER, S.P. 2019 Hypersonic ground tests with high-frequency instrumentation in support of the boundary layer transition (BOLT) flight experiment. In *AIAA Scitech 2019 Forum*, p. 0090.

BOUNITCH, A., LEWIS, D. & LAFFERTY, J. 2011 Improved measurements of 'tunnel noise' pressure fluctuations in the AEDC hypervelocity wind tunnel No. 9. In *49th AIAA Aerospace Sciences Meeting including the New Horizons Forum and Aerospace Exposition*, p. 1200.

BUCHTA, D., VISHNAMPET, R., BODONY, D.J. & FREUND, J.B. 2016 A discrete adjoint-based shape optimization for shear-layer-noise reduction. In *22nd AIAA/CEAS Aeroacoustics Conference*, p. 2776.

BULL, M.K. 1996 Wall-pressure fluctuations beneath turbulent boundary layers: some reflections on forty years of research. *J. Sound Vib.* **190** (3), 299–315.

BUSHNELL, D. 1990 Notes on initial disturbance fields for the transition problem. In *Instability and Transition* (ed. M.Y. Hussaini & R.G. Voigt), pp. 217–232. Springer.

CASPER, K.M., BERESH, S.J., HENFLING, J.F., SPILLERS, R.W., PRUETT, B.O.M. & SCHNEIDER, S.P. 2016 Hypersonic wind-tunnel measurements of boundary-layer transition on a slender cone. *AIAA J.* **54** (1), 1250–1263.

CHANG, C.L., MALIK, M. & HUSSAINI, M. 1990 Effects of shock on the stability of hypersonic boundary layers. In *21st Fluid Dynamics, Plasma Dynamics and Lasers Conference*, p. 1448.

CHANG, C.-L., MALIK, M.R., ERLEBACHER, G. & HUSSAINI, M.Y. 1993 Linear and nonlinear PSE for compressible boundary layers. NASA Contractor Report 191537. ICASE Report No 93-70.

CHAUDHRY, R.S. & CANDLER, G.V. 2017 Computing measured spectra from hypersonic pitot probes with flow-parallel freestream disturbances. *AIAA J.* **55** (12), 4155–4166.

CHEUNG, L.C. & ZAKI, T.A. 2010 Linear and nonlinear instability waves in spatially developing two-phase mixing layers. *Phys. Fluids* **22** (5), 052103.

CHYNOWETH, B.C. 2018 Measurements of transition dominated by the second-mode instability at Mach 6. PhD thesis, Purdue University.

CHYNOWETH, B.C., SCHNEIDER, S.P., HADER, C., FASEL, H., BATISTA, A., KUEHL, J., JULIANO, T.J. & WHEATON, B.M. 2019 History and progress of boundary-layer transition on a Mach 6 flared cone. *J. Spacecr. Rockets* **56** (2), 333–346.

COLBURN, C. 2011 Estimation techniques for large-scale turbulent fluid systems. PhD thesis, UC San Diego.

CORCOS, G.M. 1963 Resolution of pressure in turbulence. *J. Acoust. Soc. Am.* **35** (2), 192–199.

DUAN, L., *et al.* 2019 Characterization of freestream disturbances in conventional hypersonic wind tunnels. *J. Spacecr. Rockets* **56** (2), 357–368.

FEDOROV, A. 2011 Transition and stability of high-speed boundary layers. *Annu. Rev. Fluid Mech.* **43**, 79–95.

FRANKO, K.J. & LELE, S.K. 2013 Breakdown mechanisms and heat transfer overshoot in hypersonic zero pressure gradient boundary layers. *J. Fluid Mech.* **730**, 491–532.

FRANKO, K.J. & LELE, S.K. 2014 Effect of adverse pressure gradient on high speed boundary layer transition. *Phys. Fluids* **26** (2), 024106.

HADER, C. & FASEL, H.F. 2018 Towards simulating natural transition in hypersonic boundary layers via random inflow disturbances. *J. Fluid Mech.* **847**, R3.

HADER, C. & FASEL, H.F. 2019 Direct numerical simulations of hypersonic boundary-layer transition for a flared cone: fundamental breakdown. *J. Fluid Mech.* **869**, 341–384.

HANIFI, A., SCHMID, P.J. & HENNINGSON, D.S. 1996 Transient growth in compressible boundary layer flow. *Phys. Fluids* **8** (3), 826–837.

JAHANBAKHSHI, R. & ZAKI, T.A. 2019 Nonlinearly most dangerous disturbance for high-speed boundary-layer transition. *J. Fluid Mech.* **876**, 87–121.

KENNEDY, R.E., LAURENCE, S.J., SMITH, M.S. & MARINEAU, E.C. 2018 Investigation of the second-mode instability at Mach 14 using calibrated schlieren. *J. Fluid Mech.* **845**, R2.

KNUTSON, A.L., THOME, J.S. & CANDLER, G.V. 2021 Numerical simulation of instabilities in the boundary-layer transition experiment flow field. *J. Spacecr. Rockets* **58** (1), 90–99.

KOSTAK, H., BOWERSOX, R.D., MCKIERNAN, G., THOME, J., CANDLER, G.V. & KING, R. 2019 Freestream disturbance effects on boundary layer instability and transition on the AFOSR BOLT geometry. In *AIAA Scitech 2019 Forum*, p. 0088.

KOVASZNAY, L.S.G. 1953 Turbulence in supersonic flow. *J. Aeronaut. Sci.* **20** (10), 657–674.

LAIBLE, A. & FASEL, H. 2011 Numerical investigation of hypersonic transition for a flared and a straight cone at Mach 6. In *41st AIAA Fluid Dynamics Conference and Exhibit*, p. 3565.

LARSSON, J. & LELE, S.K. 2009 Direct numerical simulation of canonical shock/turbulence interaction. *Phys. Fluids* **21** (12), 126101.

https://doi.org/10.1017/jfm.2021.172 Published online by Cambridge University Press

LAURENCE, S.J., WAGNER, A. & HANNEMANN, K. 2016 Experimental study of second-mode instability growth and breakdown in a hypersonic boundary layer using high-speed schlieren visualization. *J. Fluid Mech.* **797**, 471–503.

LAURENCE, S.J., WAGNER, A., HANNEMANN, K., WARTEMANN, V., LÜDEKE, H., TANNO, H. & ITOH, K. 2012 Time-resolved visualization of instability waves in a hypersonic boundary layer. *AIAA J.* **50** (1), 243–246.

LI, X., FU, D. & MA, Y. 2010 Direct numerical simulation of hypersonic boundary layer transition over a blunt cone with a small angle of attack. *Phys. Fluids* **22** (2), 025105.

LIU, C., XIAO, Q. & WANG, B. 2008 An ensemble-based four-dimensional variational data assimilation scheme. Part I: technical formulation and preliminary test. *Mon. Weath. Rev.* **136** (9), 3363–3373.

LORENZ, E.N. 1963 Deterministic nonperiodic flow. *J. Atmos. Sci.* **20** (2), 130–141.

LUEPTOW, R.M. 1995 Transducer resolution and the turbulent wall pressure spectrum. *J. Acoust. Soc. Am.* **97** (1), 370–378.

LYSENKO, V.I. & MASLOV, A.A. 1984 The effect of cooling on supersonic boundary-layer stability. *J. Fluid Mech.* **147**, 39–52.

MACK, L.M. 1975 Linear stability theory and the problem of supersonic boundary-layer transition. *AIAA J.* **13** (3), 278–289.

MACK, L.M. 1984 Boundary-layer linear stability theory. *Tech. Rep.* California Inst of Tech Pasadena Jet Propulsion Lab.

MALIK, M.R. 1990 Numerical methods for hypersonic boundary layer stability. *J. Comput. Phys.* **86** (2), 376–413.

MARINEAU, E.C., GROSSIR, G., WAGNER, A., LEINEMANN, M., RADESPIEL, R., TANNO, H., CHYNOWETH, B.C., SCHNEIDER, S.P., WAGNILD, R.M. & CASPER, K.M. 2019 Analysis of second-mode amplitudes on sharp cones in hypersonic wind tunnels. *J. Spacecr. Rockets* **56** (2), 307–318.

MARINEAU, E.C., MORARU, G.C., LEWIS, D.R., NORRIS, J.D., LAFFERTY, J.F. & JOHNSON, H.B. 2015 Investigation of Mach 10 boundary layer stability of sharp cones at angle-of-attack, Part I: experiments. In *53rd AIAA Aerospace Sciences Meeting*, p. 1737.

MARINEAU, E.C., MORARU, G.C., LEWIS, D.R., NORRIS, J.D., LAFFERTY, J.F., WAGNILD, R.M. & SMITH, J.A. 2014 Mach 10 boundary layer transition experiments on sharp and blunted cones. In *19th AIAA International Space Planes and Hypersonic Systems and Technologies Conference*, p. 3108.

MASUTTI, D., SPINOSA, E., CHAZOT, O. & CARBONARO, M. 2012 Disturbance level characterization of a hypersonic blowdown facility. *AIAA J.* **50** (12), 2720–2730.

MONS, V., CHASSAING, J.C., GOMEZ, T. & SAGAUT, P. 2016 Reconstruction of unsteady viscous flows using data assimilation schemes. *J. Comput. Phys.* **316**, 255–280.

MONS, V., WANG, Q. & ZAKI, T.A. 2019 Kriging-enhanced ensemble variational data assimilation for scalar-source identification in turbulent environments. *J. Comput. Phys.* **398**, 108856.

PARK, J. & ZAKI, T.A. 2019 Sensitivity of high-speed boundary-layer stability to base-flow distortion. *J. Fluid Mech.* **859**, 476–515.

PARZIALE, N.J., SHEPHERD, J.E. & HORNUNG, H.G. 2014 Free-stream density perturbations in a reflected-shock tunnel. *Exp. Fluids* **55** (2), 1665.

PARZIALE, N.J., SHEPHERD, J.E. & HORNUNG, H.G. 2015 Observations of hypervelocity boundary-layer instability. *J. Fluid Mech.* **781**, 87–112.

PATE, S.R. 1980 Effects of wind tunnel disturbances on boundary-layer transition with emphasis on radiated noise: a review. *Tech. Rep.* ARO INC ARNOLD AFS TN.

PHILLIPS, O.M. 1960 On the generation of sound by supersonic turbulent shear layers. *J. Fluid Mech.* **9** (1), 1–28.

PINNA, F. & RAMBAUD, P. 2013 Effects of shock on hypersonic boundary layer stability. *Prog. Flight Phys.* **5**, 93–106.

PRUETT, C.D. & CHANG, C.-L. 1998 Direct numerical simulation of hypersonic boundary-layer flow on a flared cone. *Theor. Comput. Fluid Dyn.* **11** (1), 49–67.

RESHOTKO, E. 1976 Boundary-layer stability and transition. *Annu. Rev. Fluid Mech.* **8** (1), 311–349.

SALTZMAN, B. 1962 Finite amplitude free convection as an initial value problem—I. *J. Atmos. Sci.* **19** (4), 329–341.

SARIC, W.S., REED, H.L. & KERSCHEN, E.J. 2002 Boundary-layer receptivity to freestream disturbances. *Annu. Rev. Fluid Mech.* **34** (1), 291–319.

SCHNEIDER, S.P. 2001 Effects of high-speed tunnel noise on laminar-turbulent transition. *J. Spacecr. Rockets* **38** (3), 323–333.

SCHNEIDER, S.P. 2015 Developing mechanism-based methods for estimating hypersonic boundary-layer transition in flight: the role of quiet tunnels. *Prog. Aerosp. Sci.* **72**, 17–29.

https://doi.org/10.1017/jfm.2021.172 Published online by Cambridge University Press

DA SILVA, A.F.C. & COLONIUS, T. 2018 Ensemble-based state estimator for aerodynamic flows. *AIAA J.* **56** (7), 2568–2578.

SIVASUBRAMANIAN, J. & FASEL, H.F. 2015 Direct numerical simulation of transition in a sharp cone boundary layer at Mach 6: fundamental breakdown. *J. Fluid Mech.* **768**, 175–218.

THIELE, T., GÜLHAN, A. & OLIVIER, H. 2018 Instrumentation and aerothermal postflight analysis of the rocket technology flight experiment ROTEX-T. *J. Spacecr. Rockets* **55** (5), 1050–1073.

THOME, J., DWIVEDI, A., NICHOLS, J.W. & CANDLER, G.V. 2018 Direct numerical simulation of BOLT hypersonic flight vehicle. In *2018 Fluid Dynamics Conference*, p. 2894.

UCINSKI, D. 2004 *Optimal Measurement Methods for Distributed Parameter System Identification*. CRC Press.

VISHNAMPET, R., BODONY, D.J. & FREUND, J.B. 2015 A practical discrete-adjoint method for high-fidelity compressible turbulence simulations. *J. Comput. Phys.* **285**, 173–192.

WANG, M., WANG, Q. & ZAKI, T.A. 2019*a* Discrete adjoint of fractional-step incompressible Navier–Stokes solver in curvilinear coordinates and application to data assimilation. *J. Comput. Phys.* **396**, 427–450.

WANG, M. & ZAKI, T.A. 2021 State estimation in turbulent channel flow from limited observations. *J. Fluid Mech.* arXiv:2011.03711.

WANG, Q., HASEGAWA, Y. & ZAKI, T.A. 2019*b* Spatial reconstruction of steady scalar sources from remote measurements in turbulent flow. *J. Fluid Mech.* **870**, 316–352.

WILSON, A.D., SCHULTZ, J.A. & MURPHEY, T.D. 2014 Trajectory synthesis for Fisher information maximization. *IEEE Trans. Robot.* **30** (6), 1358–1370.

YAN, L., DUAN, X., LIU, B. & XU, J. 2018 Bayesian optimization based on K-optimality. *Entropy* **20** (8), 594.

ZHAO, L., ZHANG, C.-B., LIU, J.-X. & LUO, J.-S. 2016 Improved algorithm for solving nonlinear parabolized stability equations. *Chin. Phys.* B **25** (8), 084701.

ZHU, Y., ZHANG, C., CHEN, X., YUAN, H., WU, J., CHEN, S., LEE, C. & GAD-EL HAK, M. 2016 Transition in hypersonic boundary layers: role of dilatational waves. *AIAA J.* **54** (10), 3039–3049.

https://doi.org/10.1017/jfm.2021.172 Published online by Cambridge University Press